

REPORT DOCUMENTATION PAGE				Form Approved OMB No. 0704-0188	
Public reporting burden for this collection of information is estimated to average 1 hour per response, including the time for reviewing instructions, searching existing data sources, gathering and maintaining the data needed, and completing and reviewing this collection of information. Send comments regarding this burden estimate or any other aspect of this collection of information, including suggestions for reducing this burden to Department of Defense, Washington Headquarters Services, Directorate for Information Operations and Reports (0704-0188), 1215 Jefferson Davis Highway, Suite 1204, Arlington, VA 22202-4302. Respondents should be aware that notwithstanding any other provision of law, no person shall be subject to any penalty for failing to comply with a collection of information if it does not display a currently valid OMB control number. PLEASE DO NOT RETURN YOUR FORM TO THE ABOVE ADDRESS.					
1. REPORT DATE (DD-MM-YYYY) 28-10-2010		2. REPORT TYPE Technical Paper		3. DATES COVERED (From - To)	
4. TITLE AND SUBTITLE Development of Terahertz Rayleigh Scattering Diagnostics For A Solid Rocket Exhaust Plume				5a. CONTRACT NUMBER	
				5b. GRANT NUMBER	
				5c. PROGRAM ELEMENT NUMBER	
6. AUTHOR(S) Anthony Thomas O'Shea				5d. PROJECT NUMBER	
				5f. WORK UNIT NUMBER 50260542	
7. PERFORMING ORGANIZATION NAME(S) AND ADDRESS(ES) Air Force Research Laboratory (AFMC) AFRL/RZSA 10 E. Saturn Blvd. Edwards AFB CA 93524-7680				8. PERFORMING ORGANIZATION REPORT NUMBER AFRL-RZ-ED-TP-2010-461	
9. SPONSORING / MONITORING AGENCY NAME(S) AND ADDRESS(ES) Air Force Research Laboratory (AFMC) AFRL/RZS 5 Pollux Drive Edwards AFB CA 93524-7048				10. SPONSOR/MONITOR'S ACRONYM(S)	
				11. SPONSOR/MONITOR'S NUMBER(S) AFRL-RZ-ED-TP-2010-461	
12. DISTRIBUTION / AVAILABILITY STATEMENT Distribution A: Approved for public release; distribution unlimited (PA #10560).					
13. SUPPLEMENTARY NOTES Master's Thesis, University of Colorado, Colorado Springs, CO.					
14. ABSTRACT This research proposes a new technique using terahertz radiation and Rayleigh scattering off of particulates in the plume. This technique is limited to firing the beam straight across the plume. Terahertz radiation wavelengths in relation to alumina particle sizes align with the Rayleigh criterion, which requires that the wavelength of light be at least ten times greater than the radius of the particle. Rayleigh scattering would allow for changing the location of the detector and even co-locating it with the source. Unfortunately, terahertz sources with the required power output are currently in production. Thus, a scaled experiment was setup using microwaves at 2.45 GHz with aluminum, brass, and stainless steel spheres of radii ranging from 4.76 mm to 9.53 mm. A magnetron power source was used to provide a power range of 200-2000 Watts into an anechoic chamber. The forward power was measured and then passed through a horn antenna, scattered off of particles, and collected in another horn antenna. The same test was performed for no spheres inside the chamber and the difference was considered the scattered power. These results were compared with predictions obtained from a Matlab code written for this research. From this experiment, it was shown that one can use Rayleigh's equations to determine particle size based on scattered power detected if the number density is known. However, the uncertainties in index of refraction and scattering efficiency as well as a low signal to noise ratio led to large error bars and discrepancies between predictions and experimental data. Also, a notional terahertz diagnostic instrument was developed that would operate at a range of 20 km using a 1 kW source and a 3m diameter parabolic reflector antenna. Further research is needed to characterize the properties of alumina especially the refractive index and scattering efficiency to ensure accurate measurements from the terahertz instrument.					
15. SUBJECT TERMS					
16. SECURITY CLASSIFICATION OF:			17. LIMITATION OF ABSTRACT SAR	18. NUMBER OF PAGES 83	19a. NAME OF RESPONSIBLE PERSON Mr. Marcus Young
a. REPORT	b. ABSTRACT	c. THIS PAGE			19b. TELEPHONE NUMBER (include area code)
Unclassified	Unclassified	Unclassified			N/A

**DEVELOPMENT OF TERAHERTZ RAYLEIGH SCATTERING DIAGNOSTICS
FOR A SOLID ROCKET EXHAUST PLUME**

by

ANTHONY THOMAS O'SHEA

B.S., United States Air Force Academy, 2009

A thesis submitted to the Graduate Faculty of the

University of Colorado at Colorado Springs

in partial fulfillment of the

requirements for the degree of

Masters of Mechanical Engineering

Department of Mechanical and Aerospace Engineering

2010

The views expressed in this article are those of the author and do not reflect the official policy or position of the United States Air Force, Department of Defense, or the U.S. Government.

© Copyright By Anthony Thomas O'Shea 2010

All Rights Reserved

Distribution A: Approved for public release. Distribution unlimited.

This thesis for a Masters of Mechanical Engineering degree by

Anthony Thomas O'Shea

has been approved for the

Department of Mechanical and Aerospace Engineering

By

Andrew Ketsdever, Chair

Rebecca Webb

Hoyoung Song

Date

O'Shea, Anthony Thomas (M.S., Mechanical Engineering)

Development of Terahertz Rayleigh Scattering Diagnostic for a Solid Rocket Exhaust Plume

Thesis directed by Assistant Professor Andrew D. Ketsdever

Characterization of rocket plumes has been difficult due to the lack of non-intrusive real-time measurement techniques. This research proposes a new technique using terahertz radiation and Rayleigh scattering off of particulates in the plume. Previous techniques have involved collecting particles on a probe or mesh. Others have used Mie scattering using lasers, but this technique is limited to firing the beam straight across the plume. Terahertz radiation wavelengths in relation to alumina particle sizes align with the Rayleigh criterion, which requires that the wavelength of light be at least ten times greater than the radius of the particle. Rayleigh scattering would allow for changing the location of the detector and even co-locating it with the source. Unfortunately, terahertz sources with the required power output are currently in production. Thus, a scaled experiment was setup using microwaves at 2.45 GHz with aluminum, brass, and stainless steel spheres of radii ranging from 4.76 mm to 9.53 mm. A magnetron power source was used to provide a power range of 200-2000 Watts into an anechoic chamber. The forward power was measured and then passed through a horn antenna, scattered off of particles, and collected in another horn antenna. This detected power was measured and recorded. The same test was performed for no spheres inside the chamber and the difference was considered the scattered power. These results were compared with predictions obtained from a Matlab code written for this research. From this experiment, it was shown that one can use Rayleigh's equations to determine particle size based on scattered power detected if the number density is known. However, the uncertainties in index of refraction and scattering efficiency as well as a low signal to noise ratio led to large error bars and discrepancies between predictions and experimental data. Also, a notional terahertz diagnostic instrument was developed that would operate at a range of 20 km using a 1 kW source and a 3m diameter parabolic reflector antenna. Further research is needed to characterize the properties of alumina especially the refractive index and scattering efficiency to ensure accurate measurements from the terahertz instrument.

DEDICATION

To my family especially Mom and Dad.

ACKNOWLEDGMENTS

This work was supported by the National Institute of Science, Space, and Security Centers, the Center for Space Studies, and the College of Engineering and Applied Science at the University of Colorado at Colorado Springs. The author wishes to thank Dr. Scott Trimboli and Dr. Dan Dandapani.

Dr. Andrew Ketsdever deserves special acknowledgement for not only accepting the author into the graduate program, but also for helping the author along this long and sometimes confusing route. His mentorship and patience have been well received and appreciated. Without Dr. Ketsdever none of this work would have been possible.

The author wishes to thank Mr. Keagen Cothorn who provided much needed assistance throughout this project. He helped immensely during the experiment phase of this study, and his work is greatly valued.

The author also wishes to thank Dr. Hoyoung Song and Mr. Jim Wigle for the use of the anechoic chamber facilities as well as numerous discussions about the physics of light transmission and measurement.

TABLE OF CONTENTS

CHAPTER

I.	INTRODUCTION	1
II.	TERAHERTZ SOURCES AND APPLICATIONS	5
	Current Sources: Capabilities and Applications	5
	Gyrotrons: Theory and Proposed Source	7
III.	SOLID ROCKET EXHAUST PLUME CHARACTERISTICS	10
	Rocket Exhaust Plume Environment	10
	Aluminum Oxide Properties	11
	Measurements and Predictions of Aluminum Oxide	13
IV.	PREVIOUS RAYLEIGH EXPERIMENTS	16
	General Rayleigh Experiments	16
	Microwave Rayleigh Experiments.....	20
V.	THEORY OF APPLIED LIGHT SCATTERING	23
	A Comparison of Mie and Rayleigh Theories	23
	Mie Scattering Theory	23
	Rayleigh Scattering Theory	24
	Antenna Theory	25
	Light Propagation Considerations.....	26
	Parabolic Reflector Antennas	28
	Horn Antennas	30
	Rayleigh Approach	31

VI.	EXPERIMENTAL SETUP AND PREDICTED RESULTS	34
	Experimental Setup.....	34
	Predicted Experimental Results	38
VII.	RESULTS AND DISCUSSION OF PROOF OF CONCEPT EXPERIMENT.....	42
	Single Sphere Results	42
	Double Sphere Results.....	43
	Sphere Number Comparison.....	45
	Sphere Size Comparison	45
	Sphere Material Comparison	47
	Experiment Discussion	48
	Sources of Error.....	48
	Differences Between Theory and Results.....	49
VIII.	DEVELOPMENT OF NOTIONAL TERAHERTZ INSTRUMENT	51
	Notional Terahertz Instrument.....	51
	Complications of Implementation for Notional Terahertz Instrument.....	53
IX.	CONCLUSION	57
	REFERENCES.....	60
	APPENDIX A: ROCKET PLUME CONSTITUENT DATA	64
	APPENDIX B: MATLAB CODE FOR EXPERIMENTAL PREDICTIONS.....	66
	APPENDIX C: MATLAB CODE FOR THZ INSTRUMENT PERFORMANCE	68

TABLES

Table

1. Proposed gyrotron source parameters ¹⁷	9
2. Index of refraction of synthetic sapphire at visible wavelengths and three temperatures ²⁴	12
3. Index of refraction dependence on wavelength and temperature ²⁵	13
4. Results from Rayleigh scattering flow diagnostics ³³	19
5. Differences between predicted and experimental results	49

FIGURES

Figure

1. Intensity ratio for several sources	5
2. Cross-section of a gyrotron beam ¹⁶	7
3. The two-phase flow environment for liquid and solid rockets ¹⁸	11
4. Comparison of particle size correlations ²⁶	14
5. Typical collection images from scanning electron microscope ¹	15
6. Dependence of argon cluster size on the backing pressure ³⁰	17
7. Results from spectrally resolved Rayleigh scattering experiment ³¹	18
8. Predicted Rayleigh scattering cross-section ³⁶	21
9. Experimental and predicted results of microwave Rayleigh scattering experiment ³⁸	22
10. Depiction of elastic light scattering	25
11. Atmospheric attenuation for given frequencies ⁴⁴	27
12. Several large reflector antennas (a) Effelsberg 100-meter radio telescope (b) ATS-6 unfurlable 300-ft reflector (c) Arecibo 1000-ft spherical reflector ⁴⁷	29
13. Horn antenna types: (a) H-plane sectoral, (b) E-plane sectoral (c) Pyramidal ⁵⁰	30
14. 2 kW magnetron source and horn antenna	35
15. Distance traveled by microwaves from transmitter	35
16. Sphere configuration (A) Single and (B) Double	36

17. Receiving horn for scattered microwaves	36
18. Experimental setup from observer perspective	37
19. Experimental setup from sphere perspective	37
20. Overhead view of experimental setup	37
21. Relation between refractive index and wavelength for aluminum	39
22. Scattered power versus source power for generic sphere with $r = 9.53$ mm and $m = 2$	40
23. Scattered power versus sphere radius with $m = 2$	40
24. Scattered power versus source power for a 9.53 mm radius sphere as a function of the refractive index	40
25. Scattered power versus source power for a fixed refractive index of $m = 10^9$	41
26. Scattered power versus source power for one aluminum sphere	42
27. Scattered power versus source power for one brass sphere	42
28. Scattered power versus source power for two aluminum spheres	43
29. Scattered power versus source power for two brass spheres	44
30. Scattered power versus source power for two stainless steel spheres	44
31. Aluminum sphere number comparison	45
32. Aluminum sphere size comparison	46
33. Brass sphere size comparison	46
34. Stainless Steel sphere size comparison	46

35. Sphere material comparison for 9.53 mm radius sphere	47
36. Sphere material comparison for 4.76 mm radius sphere	48
37. Relation between range to particle and power ratio with multiple antenna radii	52
38. Relation between antenna radius and power ratio assuming minimum range to particle	52
39. Notional terahertz diagnostic instrument	53
40. Attenuation due to water for terahertz instrument ⁴⁴	54
41. Scattered power versus source power for one aluminum sphere	55
42. Scattered power versus source power for two aluminum sphere	55
43. Scattered power versus source power for three aluminum sphere	56

NOMENCLATURE

I_s	=	scattered intensity
I_I	=	incident intensity
r	=	radius
m	=	index of refraction
λ	=	wavelength of incident light
d	=	distance from particle to detector
N	=	number density of particles
v	=	observation volume
σ_{ss}	=	scattering cross-section
$\frac{d\sigma_{ss}}{d\Omega}$	=	differential scattering cross-section
Ω	=	collection solid angle
V	=	volume of the particle
A	=	cross-sectional area of particle
ϕ	=	elevation angle
P_{det}	=	power to the detector
η	=	scattering efficiency
θ	=	rotation angle
R	=	distance from transmitter to particle
D_{dish}	=	diameter of the antenna dish
P_r	=	power received
P_t	=	power transmitted
G_r	=	gain of the receiving antenna
G_t	=	gain of the transmitting antenna
r_{dish}	=	radius of the antenna dish
f	=	frequency of light
SL	=	free space loss

CHAPTER 1

INTRODUCTION

This study seeks to further the development of a non-intrusive diagnostic instrument that can be used to characterize alumina particles in solid rocket plumes. Particle size and density in rocket plumes are difficult to measure accurately. Some current methods involve collecting particles on a screen or placing a probe into the plume itself.¹ While these methods have produced results, they require a static setup and can be subject to contamination. This study will investigate the use of terahertz radiation and the principles of Rayleigh light scattering to accurately determine particle number density, size, and velocity. Terahertz wavelengths range between 3000 μm to 30 μm and the particles inside the rocket plume are between 1 μm and 100 μm . The ratio between wavelength and particle radius satisfies the Rayleigh light scattering criterion that the wavelength must be at least ten times larger than the particle radius. Therefore, terahertz radiation is ideally suited to be used in the development of this diagnostic tool.

Since the dawn of the rocket age, scientists and engineers have wanted to accurately characterize the performance of rockets in order to find mechanisms for improvement. Most gains in performance can be realized in the combustion process of the rocket fuels inside the combustion chamber. For solid rocket motors in particular, diagnostics of properties inside the combustion chamber are especially difficult because the intense heat and pressure would destroy most measuring tools. Engineers have developed models to try and predict the chemical processes occurring inside the combustion chamber. However, these models need high fidelity experimental data for verification and validation. The solution to this issue may lie in the understanding of the rocket plume and its constituents. If one can accurately measure the size, number density, velocity, and temperatures of the particles inside the solid rocket plume, the modeled combustion process can be adjusted to meet targeted plume parameters (i.e. the data can serve as an end state for which the modeled combustion process can be adjusted to meet).

Measuring these characteristics can be difficult due to the extreme nature of the plume environment. Obtaining real-time measurements adds a greater challenge. Light scattering has the potential to provide the non-intrusive measurement tool for size, number density, and velocity of particles

in real-time. In general, particle size influences the efficiency and performance of the rocket. The goal is to have the smallest, lightest, and fastest particles generated by the combustion process, leading to a higher specific impulse and thrust. Different propellant compositions produce distinct plume particle characterizations. By adjusting these compositions, based on measured results, performance and fuel use can be optimized. This tool could be used to measure particle sizes and therefore efficiency in startup and shut down of solid rocket motors. Also, by measuring the particle size, one can compare the performance of different combustion processes.

In addition to the possibility of improved efficiency through analysis of the plume constituents, another application lies in the identification of these rockets using the plume signature. With a detailed map of the particles generated by the solid rocket motor, the manufacturer and origin of the rocket could be identified. Missile defense and early warning systems could utilize plume signatures to potentially identify any enemy threats.

Light scattering offers an effective real-time, non-intrusive diagnostic tool that can be employed for almost any solid motor. Limiting the use of light scattering to Rayleigh theory offers the advantage of sensor and source mobility due to the dipole structure of the scattered light. This advantage would also include the collocation of the sensor and source. Rayleigh theory stipulates the particle size must be ten times smaller than the wavelength of the interrogating light. This study stems from the fact that the sizes of particles in a solid rocket exhaust plume and the wavelengths of terahertz radiation meet this criterion. Using the general size distribution of alumina particles that occur in the solid rocket motor plume coupled with Rayleigh theory, a notional terahertz diagnostic instrument was developed in order to provide a baseline for performance that an instrument would need to be successful in characterizing the solid constituents of the plume. Rayleigh scattering theory was combined with free space transmission equations to generate a single equation that governs the ratio between transmitted and received power. From this equation, one can determine if a real system would have sufficient power output and antenna gain to accurately measure the scattered return from particles inside the solid rocket plume.

In order to test the feasibility of employing Rayleigh theory to the diagnostic development for the characterization of particles, a proof-of-concept experiment was developed involving microwaves at 2.45 GHz and metal spheres of several sizes and materials. The experiment was scaled based on the diagnostic

wavelength used and the sphere radius. It was designed to analyze the possibility of using Rayleigh scattering to measure particle size while determining the differences between theory and experiment. It also identified some of the complications that might occur when using a terahertz diagnostic instrument.

The terahertz region of the electromagnetic spectrum between 100 *GHz* and 10 *THz* (wavelength range from 3000 μm to 30 μm) occupies a large portion of the spectrum between the infrared and microwave bands. Compared to the relatively well-developed science and technology at microwave, optical, and x-ray frequencies, developments in the terahertz band are limited and remain relatively unexplored.² The shorter wavelengths at terahertz frequencies allow the use of smaller and lighter components, which is important in military and air-borne applications. In addition, compared to infrared and optical wavelengths, atmospheric attenuation in the terahertz region is relatively low.³

One non-intrusive light scattering technique that may be employed with the particle sizes for solid rocket motors is Mie scattering, but the setup would have to be static due to the general forward-scattered direction of Mie scattered light. Lasers have also been applied to hydrogen and oxygen rocket engines using laser and Rayleigh scattering.⁴ This study examines solid rocket motors which produce particles between 1 μm and 100 μm .⁵ For these size particles, terahertz wavelengths from 10 μm to 1 mm are ideally suited to measure the particles in the plume with Rayleigh scattering. The setup is not restricted to a static fire and could be used in a real time launch configuration. The use of Rayleigh theory also removes the large complications surrounding the application of Mie theory by simplifying the intensity ratio to a basic sixth order polynomial from a combination of several associated Legendre polynomials and Riccati-Bessel functions.

The understanding of multiphase rocket exhaust plume flows is important to many scientific and engineering applications. Chemical combustion processes involve high temperature, multiphase flows from liquid fuel injectors in internal combustion engines to plume effluents at the exit plane of a rocket nozzle. The terahertz region of the electromagnetic spectrum may have a large impact on the general understanding of these two-phase flows for particle sizes between 1 μm and 100 μm . Rayleigh and Raman spectroscopy have been used to non-intrusively diagnose homogenous and heterogeneous cluster formation, condensation, and evaporation in a high-temperature gaseous flow environment. Terahertz excitation sources bring about a new possibility to interrogate flows that otherwise could not be

investigated with normal Rayleigh or Raman techniques due to the correlation between terahertz frequencies and the range of particle size with respect to the Rayleigh criterion.

CHAPTER 2

TERAHERTZ SOURCES AND APPLICATIONS

A. Current Sources: Capabilities and Applications

Terahertz sources have seen increased development in the past decade due to the rising interest in the wide variety of applications such as space, security, and imaging. As mentioned earlier, the terahertz regime is generally held to be between 100 GHz and 10 THz. This is a region where high power sources have been difficult to develop and where a great deal of research is currently being conducted. Most terahertz sources today range in output power from single micro-Watts to tens of Watts.^{6,7} There are generally two ways to produce terahertz radiation: lasers and gyrotrons. Some laser handbooks have compiled the output powers for lasers at these frequencies.^{8,9,10} From this data and using the general Rayleigh theory equation, the ratio of scattered intensity to incident intensity was determined for each of the different laser sources. These numbers were compared with the predicted performance of a gyrotron source that will be discussed later in this chapter. The results of this comparison can be seen below in Figure 1.

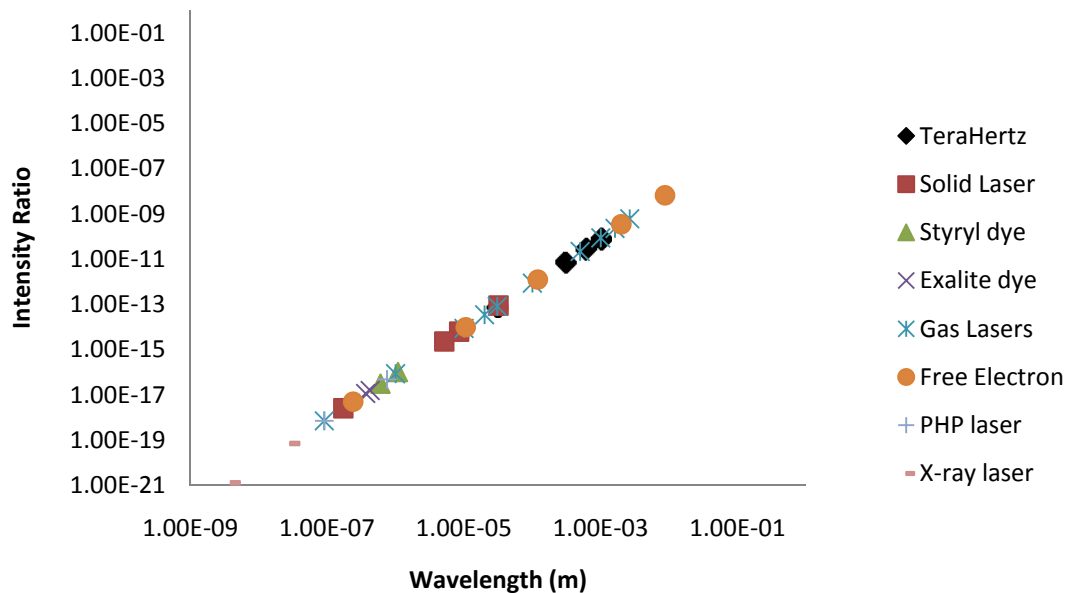


Figure 1: Intensity ratio for several sources

From this figure, one can see that only some gas lasers and free electron lasers can come close to matching the intensity ratio expected from the gyrotron source. The lasers that do match or surpass the ratio are not considered very reliable, and it will become apparent that a high output power will be required for a notional terahertz diagnostic instrument to operate effectively for this application. Also, it should be noted that many types of sources cannot attain the necessary frequency to be considered in the terahertz regime.

While current terahertz sources may not have large output powers, many applications for these relatively low power sources have been developed. One of the most prominent environments for application is in space. Many interstellar particles emit radiation in the terahertz regime. This has sparked great interest in the development of sensors that are able to characterize these emissions. This information can begin to answer questions concerning the composition and origins of the universe. Also, terahertz sensors can help characterize the atmospheric properties of other large bodies such as asteroids and comets. These characteristics can lead to improvements in the models of Earth's atmosphere.¹¹ One method of employing these space applications would be with ground stations. Gaidis¹² discusses the spaced-based application of these sensors used in the study of astronomy, atmospheric chemistry, and planetary science.

Another large area of terahertz development and application is in the imaging of objects. The area has a broad field of application including structural analysis, medical procedures, and security screening. Hu and Nuss¹³ demonstrated the ability to generate terahertz images of objects such as semiconductors. They used terahertz time-domain spectroscopy in which a pulsed laser fired into a terahertz transmitter that emitted the signal across the test specimen. The signal was collected and measured by a terahertz detector whose data was resolved into an image of the test piece. Liu *et al*¹⁴ took this concept and applied it to defense application such as the screening of packages for weapons and explosives. They demonstrated this ability by creating an image of a briefcase with a knife concealed inside and the structure of a shoe. Bogue¹⁵ discussed the improvements that have been made with terahertz applications. He explains the uses of terahertz radiation in the medical, security, and imaging fields. He also writes about the new security screening for airports that employs terahertz radiation. This study seeks to add another application for terahertz: the non-intrusive, real-time diagnostic of solid rocket exhaust plumes.

B. Gyrotrons: Theory and Proposed Source

Gyrotron devices are of great interest because of their ability to provide high average and high peak power at millimeter wavelengths which correspond to frequencies from 30 to 300 GHz. Current gyrotrons have increased the average power output generated by radio frequency (RF) sources by several orders of magnitudes. In general gyrotrons are a type of free electron maser. A gyrotron consists of vacuum tubes and magnets that bunch electrons using a strong magnetic field. A cross-section of the electron beam for a gyrotron can be seen in Figure 2.

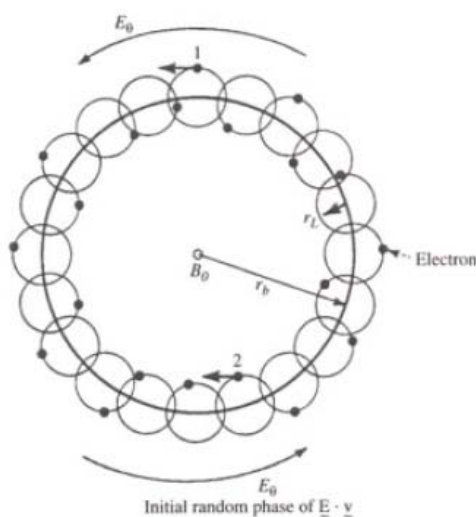


Figure 2: Cross-section of a gyrotron beam¹⁶

Basically, some electrons are decelerated by the electric field which increases their cyclotron frequency while others are accelerated and thus their cyclotron frequency decreases. This change in cyclotron frequencies causes the electrons to bunch causing transverse deceleration from which energy can be extracted. There are currently several high power gyrotron systems; one of which is a Gyromonotron oscillator. Gyrotron oscillators have been studied since the late 1960s. These machines are capable of long-duration pulses at high powers which effectively place them in a continuous wave (CW) regime. One system operates at 170 GHz with an output power between 0.5 MW and 1 MW for durations spanning from 0.5 to multiple seconds. Another state-of-the-art device is the gyrotron driven by intense relativistic electron beams (IREBs). IREBs which have very high current and high beam voltage are created by using explosive emission cathodes. They have durations less than nanoseconds per pulse. A gyro-traveling-wave-tube (TWT) mechanism was used in conjunction with IREBs in order to create a system that operates

at 35 GHz with an output power of 100 MW. Another high power system is a gyro-amplifier which can be used in millimeter-wave radar. These systems amplify the signal generated by a gyro-TWT, a gyroklystron, or a gyro-twystron to obtain high power at certain frequencies for radar application. Systems have operated around 95 GHz with output power ranging from 2.5 kW to 65 kW. Gyrotrons have also been applied to electronic counter measures (ECM). In these systems a gyro-backward-wave-oscillator (BWO) has been used. In ECM, it is important not only to have high-power but also tunability. Gyro-BWOs offer this capability and have demonstrated a frequency sweep from 27-32 GHz with an output power of 113 kW. Gyromonotron oscillators are used in industry and have shown output powers around 200 kW pulsed and 20 kW CW at a frequency of 60 GHz. Gyroklystrons can also be used to drive accelerators. Some systems have produced output powers of 100 MW at 19.76 GHz.¹⁶

The Electrical and Computer Engineering (ECE) Department at the University of Colorado at Colorado Springs has been working in conjunction with this study to develop a gyrotron system that will operate at a frequency of 300 GHz in a CW regime with an output power of 1 kW. While the power of this proposed source does not match the state-of-the-art systems mentioned above, it does have some new characteristics that make it a worthwhile pursuit. The first of these characteristics is the operating frequencies. 300 GHz lies at the low-end of the terahertz regime. This presents a unique challenge because in order to obtain this frequency the construction process will have to involve micro-fabrication techniques. This leads to the second major advantage of this system which is the compact size. Not only will the system itself be small, but the necessary magnet will also be substantially smaller. In the previous systems, the magnetic field required is rather large, thus requiring heavy and large solenoids to generate the appropriate magnetic field. This new system would only need a small periodic permanent magnet. The performance characteristics of the proposed source can be seen below in Table 1.¹⁷

Device Parameters	
Voltage	40 kV
Current	2.0 - 3.0 A
$\alpha = v_{\perp}/v_z$	1.5 - 2.0
$\Delta v_z/v_z$	5%
Magnetic field	1.1 Tesla
Operating frequency	> 300 GHz
Output power	> 1 kW
Circuit diameter	$\sim 700 \mu\text{m}$
Mode	TE _{10,1} (π mode)
Harmonic number	$s = 10$

Table 1: Proposed gyrotron source parameters¹⁷

With these two advances in gyrotron technology, the new source would be beneficial to continuing the work of this study. This source would provide the basis for characterizing the Rayleigh scattering from alumina particles so that an actual terahertz diagnostic instrument could be employed for the real-time, non-intrusive diagnostics of a solid rocket exhaust plume.

CHAPTER 3

SOLID ROCKET EXHAUST PLUME CHARACTERISTICS

With each solid rocket there are different chemical make-ups and mixtures which lead to varying performance in terms of specific impulse and total thrust. Most solid rocket motors use three basic ingredients in the propellant grain. Those ingredients are powdered aluminum as a fuel, ammonium perchlorate as an oxidizer, and hydroxyl-terminated polybutadiene as a binder for the two combustion components with varying mixture ratios. The differences in mixture ratios can lead to a variety of levels of chemical exhaust products and affects performance of the rocket. These variances in the rocket properties need to be understood in order to improve performance and efficiency, as well as optimizing prediction and modeling capabilities.

A. Rocket Exhaust Plume Environment

Inside most rocket exhaust plumes there exists a phenomenon known as two-phase flow. After the flow has expanded and cooled, gas molecules as well as solid particles constitute the flow of the plume. The ratio of solid particles to gas varies with every rocket depending on the propellant and mixtures. Also, the effect on the flow properties stems back to the varying ratios. In liquid hydrocarbon fuels, the solid phase is composed of carbon soot particles. In solid rocket motors using aluminum powder, the solid phase is comprised of aluminum oxide. The aluminum oxide particles are generally larger than soot particles. A comparison of the two rocket types and a general description of the two phase flow environment can be seen in Figure 3.¹⁸

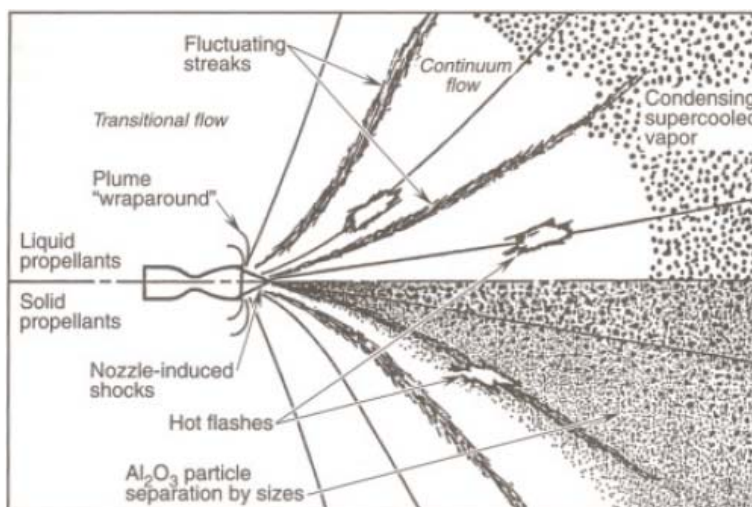


Figure 3: The two-phase flow environment for liquid and solid rockets¹⁸

In order to characterize the plume environment, several prediction codes have been developed. One code is the SPF/SIRRM which was designed to model the “nozzle flow-field, body flow-field, base/separated region, and the plume flow-field.” This code also models the radiation intensity generated by a rocket which has missile defense applications for detection and identification. However, deficiencies with the code lead to a poor handling of initial conditions in the nose region of the rocket. Another code is CHARM which is a compilation of several codes. The CHARM code performs similar functions as the SPF/SIRRM code by modeling the particles in the flow of a rocket and determining the predicted emissive properties of plumes. One shortcoming of the CHARM code is that it has difficulty accurately modeling some reaction rates in the shock layer.¹⁹ Numerical computations were also performed on a two-phase flow by Owis and Hashem.²⁰ They analyzed the effects of two-phase flow in satellite control thrusters. They numerically solved the unsteady compressible Navier-Stokes equation to determine the effects of condensing gaseous nitrogen. They found that in general this condensation lowered the thrust of the satellite control thruster. If a terahertz diagnostic instrument were built and implemented, some of the unknown parameters used in these codes could be better quantified leading to higher fidelity predictions of particle size and number density inside the exhaust plume.

B. Aluminum Oxide Properties

Aluminum oxide is the primary constituent of concern for this study. After the flow has expanded and cooled inside the solid rocket exhaust plume, aluminum oxide exists in the form of solid particles and

is sometimes referred to as alumina or synthetic sapphire. If the notional terahertz instrument is ever to be used in a real-time diagnostic of a solid rocket exhaust plume, many characteristics of alumina will have to be taken into account. The first of those characteristics will be the refractive index of alumina at the specific operating frequency. Krishnan *et al*²¹ performed an experiment to find the refractive index of liquid aluminum oxide. They used a process called laser ellipsometry which measures laser light reflected off a sample and creates a temperature difference between the two sides of the sample. Their experiment found only the real part of the refractive index. The wavelength was specific at 0.6238 μm which yielded a refractive index of 1.744 ± 0.016 . This value was used to design the notional terahertz diagnostic instrument. It should be noted that the complex index of refraction is of important value as well and is used in Mie theory calculations. Gupta and Wall²² performed an experiment using a 0.5 μm wavelength and found both the real and imaginary parts of the refractive index. They reported a complex value of $1.77+0.005i$ which illustrates the presence of the imaginary component. It should also be taken into account that there is an apparent dependence on wavelength based on the previous two reported indices. Gryvnak and Burch²³ conducted experiments to try to relate the index of refraction to both wavelength and temperature. Malitson, Murphy, and Rodney²⁴ also looked at the same relation, but at lower temperatures. They generated the following data in Table 2 for various wavelengths and temperatures.

Wavelength (μm)	17.0°C	24.0°C	31.0°C
0.7065	1.76294	1.76303	1.76312
0.6438	1.76538	1.76547	1.76556
0.5791	1.76862	1.76871	1.76880
0.5770	1.76814	1.76883	1.76892
0.5461	1.77068	1.77077	1.77086
0.4358	1.78110	1.78120	1.78130
0.4047	1.78572	1.78582	1.78592

Table 2: Index of refraction of synthetic sapphire at visible wavelengths and three temperatures²⁴

Using this data combined with the results from Gryvnak and Burch, Plass²⁵ was able to generate data for refractive index of aluminum oxide at higher temperatures. The real part of the index was assumed to be increased by $2.9 \times 10^{-5}/^\circ\text{C}$. The results are shown in Table 3.

Wavelength (μ)	n_1				
	Temperature				
	1200°C	1500°C	1600°C	1700°C	2020°C
0.5	1.805	1.814	1.817	1.82	1.83
1	1.785	1.794	1.797	1.80	1.81
2	1.775	1.784	1.787	1.79	1.80
3	1.745	1.754	1.757	1.76	1.77
4	1.715	1.724	1.727	1.73	1.74
5	1.665	1.674	1.677	1.68	1.69
6	1.575	1.584	1.587	1.59	1.60

Wavelength (μ)	n_2				
	Temperature				
	1200°C	1500°C	1600°C	1700°C	2020°C
0.5	1.8×10^{-7}	5.2×10^{-7}	1.1×10^{-6}	1.6×10^{-6}	1.2×10^{-6}
1	6.0×10^{-8}	4.4×10^{-7}	1.1×10^{-6}	1.8×10^{-6}	1.6×10^{-6}
2	5.3×10^{-8}	3.8×10^{-7}	1.0×10^{-6}	1.9×10^{-6}	2.2×10^{-6}
3	1.9×10^{-7}	8.4×10^{-7}	1.7×10^{-6}	2.4×10^{-6}	3.6×10^{-6}
4	1.4×10^{-5}	2.0×10^{-5}	2.4×10^{-5}	2.9×10^{-5}	3.5×10^{-5}
5	1.6×10^{-4}	2.3×10^{-4}	2.8×10^{-4}	3.2×10^{-4}	3.7×10^{-4}
6	9.1×10^{-4}	1.1×10^{-3}	1.4×10^{-3}	1.6×10^{-3}	1.9×10^{-3}

Table 3: Index of refraction dependence on wavelength and temperature²⁵

In the above table n_1 and n_2 represent the real and imaginary components of the complex index of refraction. From these two tables, it is obvious that before any diagnostic of solid rocket exhaust plumes can be performed using the notional terahertz diagnostic instrument, the optical properties of alumina in the terahertz regime must be fully characterized. The refractive index must be determined for the operating wavelengths as well as the temperature dependence characterized for terahertz radiation. The refractive index plays an important part in the determination of the scattering cross-section which is part of the determination of the power ratio in both Mie and Rayleigh theories. No known values for the index of refraction of alumina at terahertz wavelengths and temperatures inside the plume have been found in the literature. These values would be needed for the successful operation of a terahertz diagnostic instrument.

C. Measurements and Predictions of Aluminum Oxide

Over the years, many solid rocket launches have yielded data on the particles generated from the combustion process. One prominent paper collected data from many sources in order to compile data about aluminum oxide particle size. R.W. Hermesen²⁶ used data generated between 1962-1978 to construct a large table of data including 60 different motor, propellant, and chamber pressure varieties. The complete set of data from this comparison can be seen in Appendix A. From this table along with other prediction data, Hermesen was able to generate a single chart which relates the mean aluminum oxide particle diameter to the throat diameter of the solid rocket nozzle as in Figure 4.

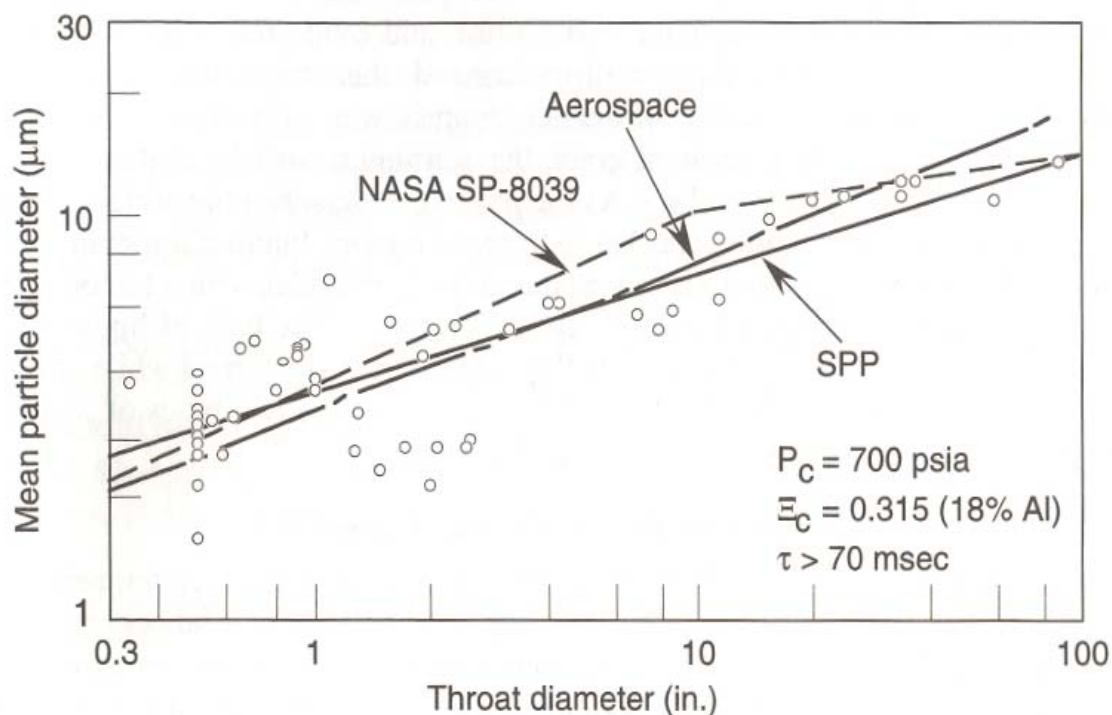


Figure 4: Comparison of particle size correlations²⁶

One type of aluminum oxide particle measurement technique calls for inserting a probe into the exhaust plume for a known amount of time and then measuring the collected particles. Laredo *et al*²⁷ collected particles in two different ways. One was scraping the particles from the walls of the nozzle and combustion chamber while the other involved a stainless steel wedge covered in a copper sheet. This probe used a flat front with tapered sides and was inserted into the exhaust plume for 0.5s. Once the collection was completed, the sample was immediately analyzed using a scanning electron microscope. Afterwards, the data was compiled and graphed.

Other engineers have strived to generate new measurements and measurement techniques to determine aluminum oxide particle size. J. K. Sambamurthi¹ developed a new probe device to enter into the exhaust plume environment and collect the particles as the rocket is firing in a static position. He developed a system that launched collection darts through the exhaust plume. Each of the darts was covered with a copper tape that collected the particles during its duration in the plume. After the rocket had been fired and the data samples collected, the copper tapes from the dart were analyzed using a scanning electron microscope. Figure 5 shows images of a typical collection tape when viewed under a microscope.

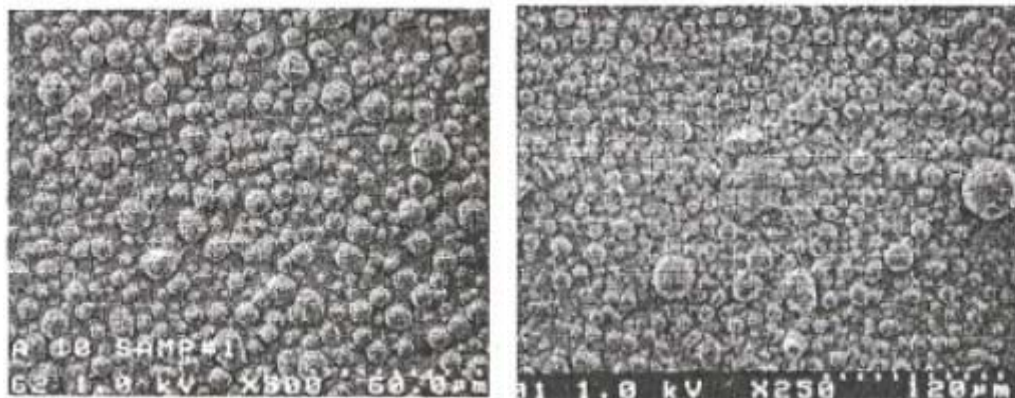


Figure 5: Typical collection images from scanning electron microscope

From the data, Sambamurthi concluded that the particles collected are mostly spherical and have a variety of different sizes. This dart system and its data may prove to be beneficial in the validation stages of an actual terahertz diagnostic system.

In addition to aluminum oxide particle measurements, the prediction of the particles' characteristics based on the properties of the solid rocket motor has become a field of interest. O. B. Kovalev²⁸ has developed prediction methods for motor and plume particle size. This prediction model relies on some previous models, but in general creates a new model which advances the modeling of agglomerate particles that enter the flow. He validates his model against the data generated by R.W. Hermesen's study and finds that his model is in line with historical data. Some other models for particle size distribution and particle density include the model developed in Reference 29 where the author develops a model based on historical data collected from actual launches at altitudes in the stratosphere. Using this data, he adjusted the model to generate similar results for particle size and number density. These models could be validated by data obtained by an actual terahertz diagnostic system.

CHAPTER 4

PREVIOUS RAYLEIGH EXPERIMENTS

In theory, Rayleigh scattering experiments can be performed with any kind of electromagnetic radiation or light. The only consideration that must be made when trying to perform a Rayleigh scattering experiment is the size of the particles. This property of the particles will dictate what wavelengths can be used for Rayleigh scattering. The criterion is that the particle radius must be at least ten times smaller than the wavelength of the interrogating light.

A. General Rayleigh Experiments

In the past, there have been many experiments to measure very small molecules and clusters of atoms. Since the small size allows for a small wavelength while still satisfying the Rayleigh criterion, there have been several experiments using lasers which tend to have wavelengths in the 100 to 1000 nanometer range. In Reference 30, the investigators were able to demonstrate the capability of measuring the size of argon clusters using Rayleigh scattering. In the experiment, they created atomic clusters by flowing argon gas through a nozzle into a vacuum environment using adiabatic expansion. In order to further simplify the Rayleigh scattering theory, they related the number density of the argon clusters to the reservoir pressure assuming that all of the argon had formed into clusters. The experiment used a pulsed Nd:YAG laser at a wavelength of 532 nm to generate the Rayleigh scattered light. The laser output was less than 1 mJ with a 15 ns pulse. The stray reflected light was absorbed in order to prevent interference with the measurements. The results from the experiment can be seen in Figure 6.

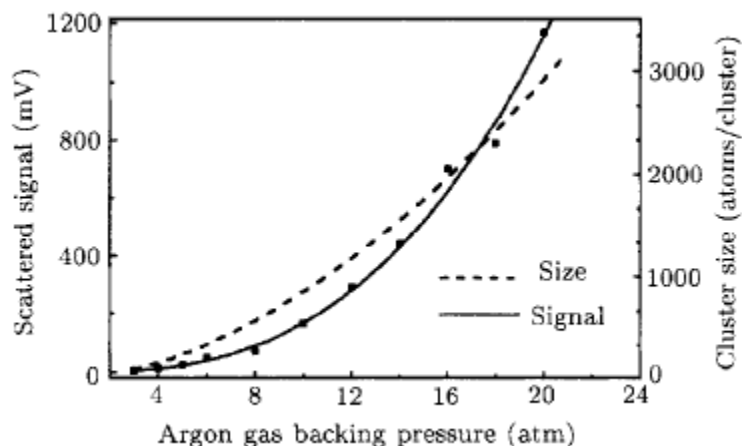


Figure 6: Dependence of argon cluster size on the backing pressure³⁰

The authors were successful in showing through Rayleigh scattering that the size of atomic argon clusters is directly dependent upon the reservoir pressure.

Seasholtz, Zupanc, and Schneider³¹ also use Rayleigh scattering as a diagnostic tool. They show the capability to measure gas density, temperature, and velocity in a hydrogen-oxygen rocket exhaust plume. Their diagnostic focuses on resolving the Rayleigh scatter spectrum. In order to accomplish this task, they utilize a Fabry-Perot interferometer. The experiment was performed using a 100 N thruster with a chamber pressure of 690 kPa and an exit pressure of 2.1 kPa. These pressures generated a mean free path of about 20 μm . This led the team to apply collisionless Rayleigh scattering theory. The source used was a 1 W argon-ion laser with a wavelength of 514.5 nm. The laser was fired into the rocket exhaust plume and then terminated after the plume. The scattered light was collected and sent through the Fabry-Perot interferometer and then into a photo-multiplier tube. The tests ran for 100s after which the collected data is processed and then plotted. Figure 7 shows the results of the experiments with different oxidizer to fuel ratios compared with JANNAF-TDK code.

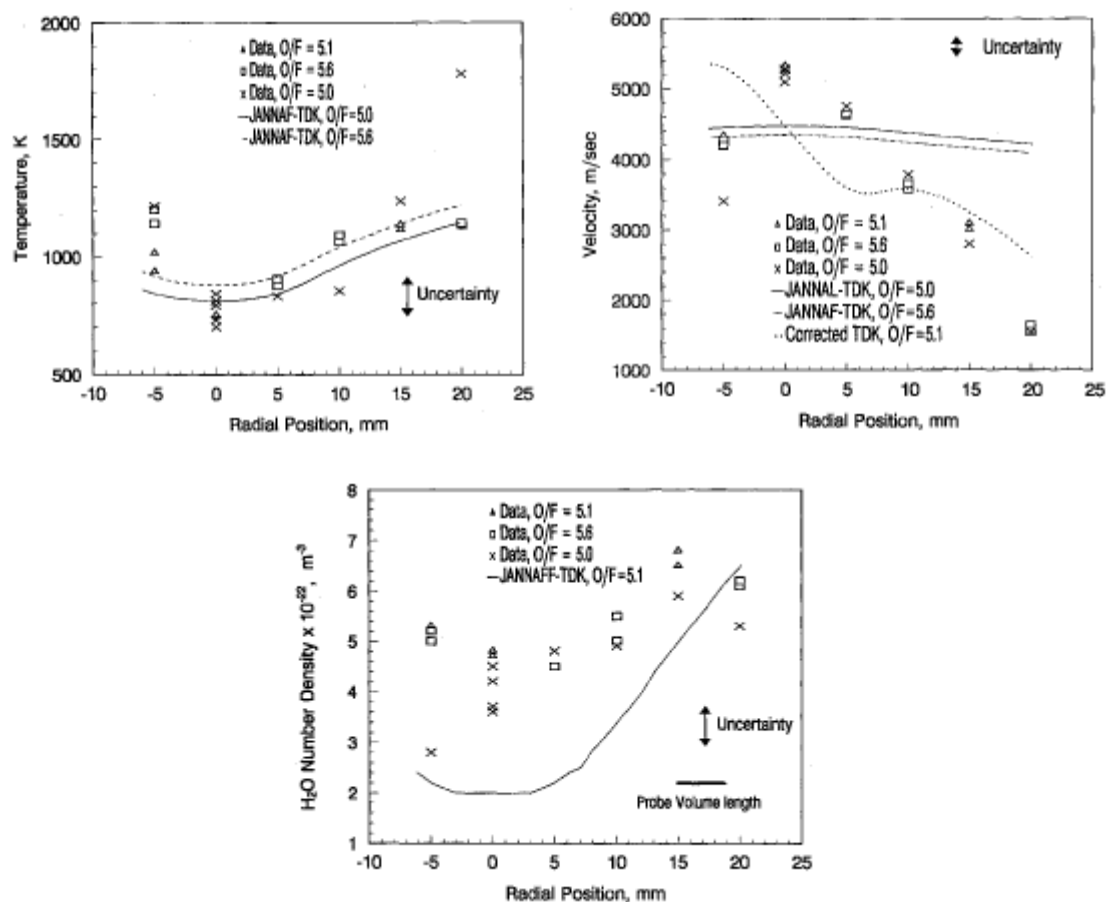


Figure 7: Results from spectrally resolved Rayleigh scattering experiment³¹

Seasholtz, Zupanc, and Schneider also discuss some sources of error that arose in their experiment. One of the most prominent sources were thermal broadening coupled with spectral broadening of the Rayleigh scattered light which led to an increase in the measured temperature. Another error source was excess hydrogen gas in the flow which increased the measured number density. Such factors will also have to be addressed in the application of terahertz diagnostics to solid rocket exhaust plumes.

Zupanc³² continued research in this area and performed a follow-on experiment that involved using pulsed laser light to interrogate a plume. He focused on determining the exit plane velocity for a small scale hydrogen-oxygen rocket. He relied on Rayleigh scattering light and the Doppler shift of the scattered light in order to make his measurements. The data was compared with the predictions RK/RPLUS code which is a full Navier-Stokes model. The radial results were in good agreement, but there were large errors associated with the axial results.

Seasholtz also continued his use of Rayleigh scattering as a diagnostic technique along with Buggele and Reeder³³. The new experiment was designed to again use Rayleigh scattered light along with a Fabry-Perot interferometer to perform flow diagnostics for a supersonic wind tunnel. The main motivation for the experiment lies in the non-intrusive nature of a Rayleigh scattering diagnostic. Conventional probes affected the flow too much to produce accurate results. Therefore, the team used a Nd:YAG laser at a wavelength of 532 nm. The laser was fired into the flow in single bursts and collected at a scattering angle of 88.9 degrees. The data was then post-processed to determine the flow characteristics. The team assumed that the flow was adiabatic for the generation of their results which can be seen in Table 4. The measurements were made at two separate points in the flow: in front of and behind a shock.

Parameter	RDG 1298	RDG 1300
Mass flow rate	13 lb ms ⁻¹	16 lb ms ⁻¹
Total temperature T7 (plenum)	296K	296K
Total pressure P7 (plenum)	16.9 psia	21.5 psia
Static pressure P8	6.28 psia	7.37 psia
Mach number MW (wedge probe)	1.95	1.95
Mach number MN3	0.94	1.00
Mean velocity (std dev) - Rayleigh	414 (51) ms ⁻¹	445 (42) ms ⁻¹
Mean temperature (std dev) - Rayleigh	209 (21)K	196 (18) K
Mean Mach number (std dev) - Rayleigh	1.44 (0.26)	1.60 (0.22)

Table 4: Results from Rayleigh scattering flow diagnostics³³

One problem that was encountered was the long amount of time that was required to post-process the data. The authors concluded that a faster method is needed for this diagnostic technique.

Seasholtz in conjunction with Panda³⁴ extended this work to characterize the velocity and temperature inside a supersonic free jet using spectrally resolved Rayleigh scattered light. The approach in the experiment utilizes a CW laser along with a Fabry-Perot interferometer and photo multiplier tubes. The power source was a 5 W Nd:YVO4 laser that operated at 532 nm. The light was transmitted into the jet stream and then collected and sent through the interferometer and the photo multiplier tubes. With this

setup, the team was able to demonstrate the capability to measure temperature and velocity in both axial and radial direction inside a Mach 0.99 and Mach 1.395 jet stream.

Another experiment that employed Rayleigh scattering to determine the size of a substance was conducted by Zhang *et al.*³⁵ In this test, the researchers set out to determine the size of glycogen that agglomerates in a solution. They use a laser spectrometer that uses a 200 mW argon-ion laser at 514.5 nm. A spectrofluorometer was also used to measure the light scattering intensity of the solution. Using these two instruments, the team was able to show the presence of glycogen in a solution and measure the average hydro-dynamic radius of the glycogen. These Rayleigh diagnostic experiments lend credibility to the feasibility of successfully conducting the proof-of-concept experiment and the application of the notional terahertz diagnostic instrument to the characterization of solid rocket exhaust plumes.

B. Microwave Rayleigh Experiments

Previous experiments involving microwave frequencies and using the principles of Rayleigh scattering are of great interest to this study given the similar nature of the proof-of-concept experiment. Many of these experiments involve a diagnostic of a plasma which while different from strictly particles, still provides insight into the workings and complications surrounding the use of Rayleigh scattering. Shneider and Miles³⁶ began using Rayleigh scattering with microwave frequencies to investigate the properties of small plasma objects. Their study developed a method that could be used as a diagnostic for small scale plasmas such as laser sparks, avalanche-streamer transitions, and resonance-enhanced multi-photon ionizations processes. They treated a plasma as a source of scattered dipole radiation when it encounters incident microwave radiation. This principle sets up the use of Rayleigh scattering theory to predict the intensity of the scattered light and the scattering cross-section of the plasma. Once they developed their equations for the total averaged power radiated by the dipole and the scattering cross-section, they generated plots of the predicted cross-section of the plasma using simulated incident intensity at frequencies of 3 and 6 GHz. The predicted results can be seen in Figure 8.

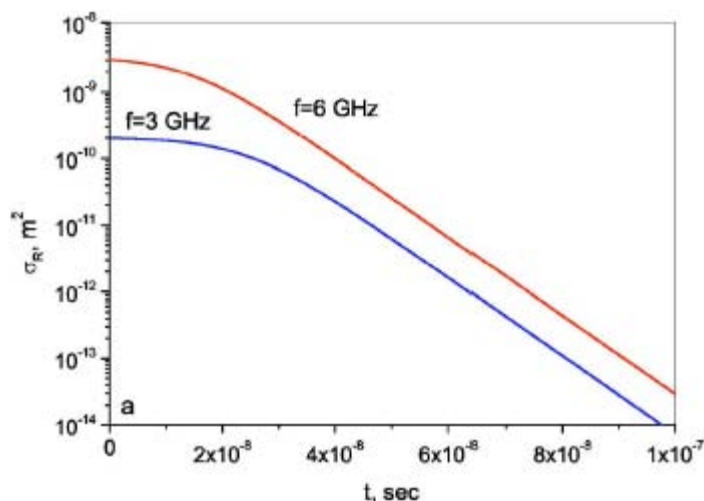


Figure 8: Predicted Rayleigh scattering cross-section³⁶

The methods developed can be used to measure the electron number density and electron-loss rate in the plasma based on the Rayleigh scattered signal.

In Reference 37, the authors apply the theories developed in Reference 36. Their study worked to conduct diagnostics of laser-induced avalanche ionization in air using microwaves and Rayleigh scattering. The team first develops equations for predicting the results from the experiment. They develop formulas for the scattering cross-section of the laser spark. Once the formulas are obtained, graphs are generated for the predicted number of electrons in the laser spark. Once predictions are finalized, the experiment is set up. In order to generate the laser breakdown in air, a Nd:YAG laser was used. For the scattering setup a tunable Gunn-diode power source was used with an output power of 15 mW at a frequency of 12.6 GHz. The power was transmitted through a WR75 horn which was 30 cm away from the laser breakdown. After the light had scattered it was collected in three WR75 receiving horns. The recorded data was processed and was found to be in good agreement with the predicted results. Thus, microwaves and Rayleigh scattering were shown to be a useful diagnostic technique for laser-induced avalanche ionization in air.

In Reference 38, the investigators continued their research using microwaves and Rayleigh scattering in order to detect resonance-enhanced multiphoton ionization in argon. Their first steps were to generate the theory for predicting the amount of microwave scattering expected from the ionization in argon. Once the theory had been established, they set up an experiment use a Ti:sapphire laser at 261.27 nm to create the ionization. To generate and measure the scattering, a 10 mW microwave source at 12.6

GHz, which corresponds to a wavelength of 2.3 cm, was used along with WR75 horns. After the test was completed the recorded data was compared with the predicted results which can be seen in Figure 9.

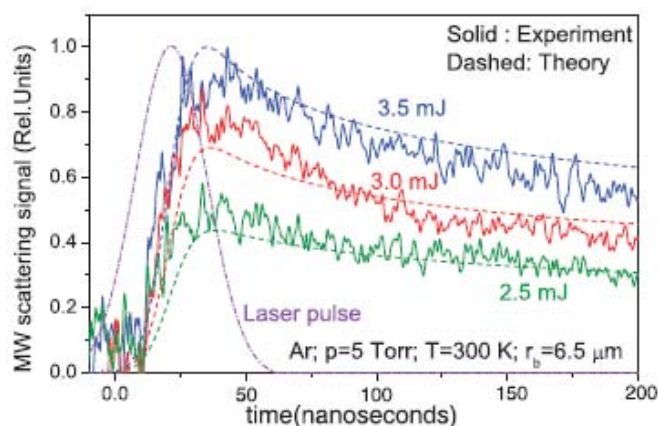


Figure 9: Experimental and predicted results of microwave Rayleigh scattering experiment³⁸

One can see from Figure 9 that the experimental results and theory are in good agreement. Thus, the team was able to conclude that with their diagnostic technique they can successfully detect resonance-enhanced multiphoton ionization in argon using Rayleigh scattering.

CHAPTER 5

THEORY OF APPLIED LIGHT SCATTERING

A. A Comparison of Mie and Rayleigh Theories

1. Mie Scattering Theory

Mie theory is an elastic light scattering theory that was developed by Gustav Mie and has sometimes been referred to as Mie-Lorenz theory. Mie started with Maxwell's equations and resolved them into equations that related the scattered light to incident light as well as defined cross-sections for scattering and absorption. The equations that are most pertinent to this study involve the relation between the scattered intensity from a spherical scattering center to the incident light that interacts with the scattering center. Van de Hulst³⁹ has given a concise summary of this theory, and the final equation for a single spherical scattering particle can be seen below

$$I_s = \frac{I_0(i_1 + i_2)}{2k^2 d^2} \quad (1)$$

k is related to the wavelength of the incident light by

$$k = \frac{2\pi}{\lambda} \quad (2)$$

The two i terms are defined by the amplitude functions for the scattered light by

$$i_1 = |S_1(\theta)|^2 \quad (3)$$

$$i_2 = |S_2(\theta)|^2 \quad (4)$$

These amplitude functions can be defined as

$$S_1(\theta) = \sum_{n=1}^{\infty} \frac{2n+1}{n(n+1)} \{a_n \pi_n(\cos \theta) + b_n \tau_n(\cos \theta)\} \quad (5)$$

$$S_2(\theta) = \sum_{n=1}^{\infty} \frac{2n+1}{n(n+1)} \{b_n \pi_n(\cos \theta) + a_n \tau_n(\cos \theta)\} \quad (6)$$

The coefficients a and b are defined using Riccati-Bessel functions by the equations

$$a_n = \frac{\varphi'_n(y)\varphi_n(x) - m\varphi_n(y)\varphi'_n(x)}{\varphi'_n(y)\zeta_n(x) - m\varphi_n(y)\zeta'_n(x)} \quad (7)$$

$$b_n = \frac{m\varphi'_n(y)\varphi_n(x) - \varphi_n(y)\varphi'_n(x)}{m\varphi'_n(y)\zeta_n(x) - \varphi_n(y)\zeta'_n(x)} \quad (8)$$

The functions φ and ζ are defined by Bessel functions by the following

$$\varphi_n(z) = \sqrt{\frac{\pi z}{2}} J_{n+1/2}(z) \quad (9)$$

$$\zeta_n(z) = \sqrt{\frac{\pi z}{2}} H_{n+1/2}^{(2)}(z) \quad (10)$$

The values for x and y are

$$x = kr \quad (11)$$

$$y = mkr \quad (12)$$

The coefficients π and τ from Eq. (5) and Eq. (6) are represented by associated Legendre polynomials by the following relations

$$\pi_n(\cos \theta) = \frac{1}{\sin \theta} P_n^1(\cos \theta) \quad (13)$$

$$\tau_n(\cos \theta) = \frac{d}{d\theta} P_n^1(\cos \theta) \quad (14)$$

Using this theory for the relation between incident light and scattered light, one can determine the size of an arbitrary spherical particle regardless of the wavelength of the incident light.

2. Rayleigh Scattering Theory

Rayleigh scattering is attributed to Sir John Rayleigh who is well known for describing the blue color of the sky. He concluded that the ratio of scattered light intensity to incident light intensity is proportional to the sixth power of the particle radius and inversely proportional to the distance from the particle squared and the fourth power of the wavelength of light. Rayleigh scattering is elastic scattering where the frequency of scattered light is equivalent to the frequency of the incident light. Fundamentally, Rayleigh scattering is an approximation of the overarching theory of Mie scattering which is also elastic in nature. However, there is one important limitation on Rayleigh scattering. The particle's radius must be at least ten times smaller than the wavelength of the incident light. If the particle is any larger the theory does not conform to the values obtained using Mie theory. An advantage of Rayleigh scattering over Mie scattering is the relative simplicity in calculating predicted scattered powers. Mie theory is a complicated process involving either several infinite sums of Legendre polynomials or multiple infinite sums of Bessel

functions of several kinds and Hankel functions. Rayleigh theory simplifies the Mie theory equations into one simple ratio of scattered intensity (I_s) to incident intensity (I_o)^{40,41}

$$\frac{I_s}{I_I} = \frac{16\pi^4 r^6 \left(\frac{m^2 - 1}{m^2 + 2}\right)^2}{\lambda^4 d^2} \quad (15)$$

The scattered intensity represented in Eq. (15) is the total intensity of light scattered from the particle. If one wants to detect scattered light, only a portion of this light will end up at a given sensor. The solid angle of the sensor's collection aperture must be taken into account using the following equation.

$$I_s = \int_0^\Omega N v I_o \frac{d\sigma_{ss}}{d\Omega} \quad (16)$$

This integral can be used to determine either the mean size of particles or the number density of particles with a certain size.

Another property of light scattering in the Rayleigh regime is the scattered intensity has an almost uniform dispersion. In the Mie regime the scattered intensity tends to be in the same direction as the incident light. This fact gives an experiment using the Rayleigh regime of scattered light more flexibility in set up because more light can be easily detected in a wide variety of sensor locations. Figure 10 illustrates the difference in scattering patterns between Mie and Rayleigh.

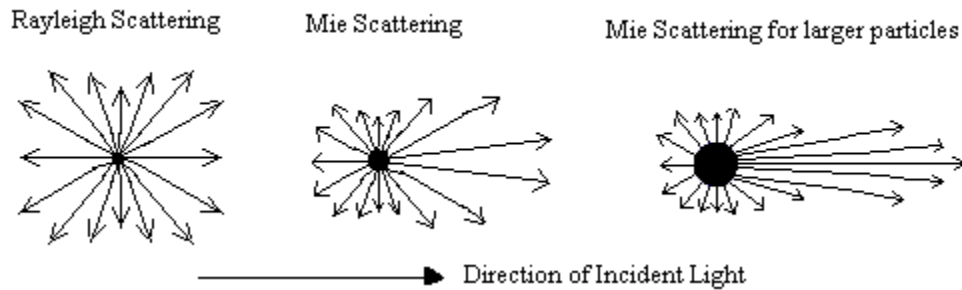


Figure 10: Depiction of elastic light scattering

B. Antenna Theory

An important characteristic of any transmitting device is the antenna used to transmit the radiation. An antenna offers a method of directionalizing the emitted radiation in order to combat the large losses that are accrued when propagating through free space. This directionality is defined in terms of an antenna's gain. A high gain corresponds to a very acute directional ability, while a small gain tends toward limited

directional capabilities. There are many different antenna types that range from simple dipole antennas with very small gain and therefore very limited directional ability to massive parabolic reflectors such as the deep space communications antennas which offer very high gain and are therefore very directional in nature. Each different antenna has its advantages and disadvantages for its specific purpose.

In this study to develop a diagnostic tool for using terahertz radiation to interrogate a solid rocket exhaust plume, two different antenna types were investigated. For the notional terahertz diagnostic instrument, a parabolic reflector was selected due to the ability to achieve the high gains required. For the proof-of-concept experiment using microwaves, horn antennas were selected for the ease of use and procurement. Both antenna types will be discussed below.

1. Light Propagation Considerations

Anytime light is generated or emitted it must travel through free space. The intensity of the light, and thus its power, is inversely proportional to the square of the distance traveled. This natural occurrence of loss is deemed free-space loss and is an issue that must be dealt with in every kind of transmitting piece of equipment from radios to televisions and especially satellite communications. To combat these losses, engineers and scientists have developed antennas to create a directional signal and allow more of the original transmitted power to be preserved. However, in order to know what antenna to use and how directional it must be, the system losses must be understood. The free space loss was characterized using the following equation.⁴²

$$SL = \left(\frac{4\pi R}{\lambda} \right)^2 \quad (17)$$

This would account for the free space loss of light, but another consideration must also be acknowledged in terms of attenuation of a signal: atmospheric interference. Many studies have looked at the problem of atmospheric attenuation and developed graphs depicting the atmospheric windows for transmitted radiation while minimizing losses.⁴³ Figure 11 below shows one graph that highlights the specific region in which the terahertz source in development would operate.⁴⁴

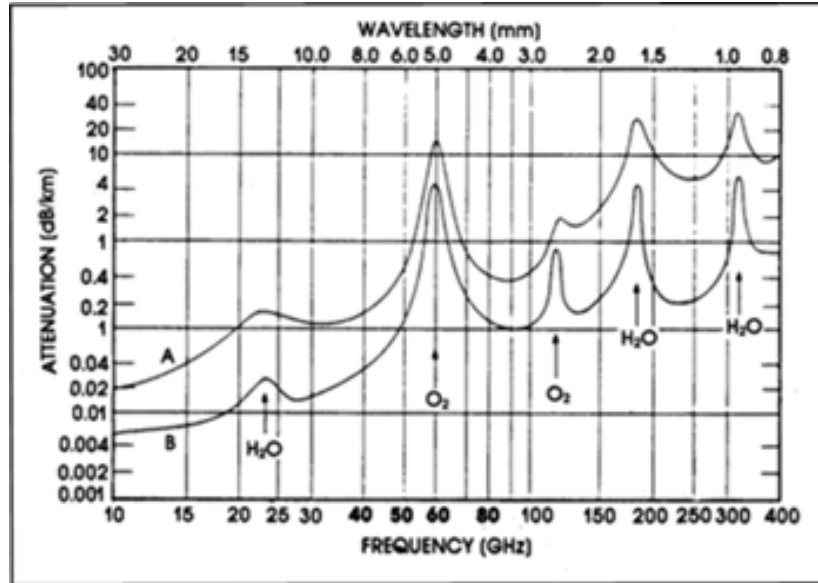


Figure 11: Atmospheric attenuation for given frequencies⁴⁴

One can see from Figure 11 that the operating frequency of 300 GHz, while on the rise of a relative lull of atmospheric attenuation still misses the peak of attenuation. Thus, this frequency lends well to be used for long-range transmission in order to interrogate a solid rocket exhaust plume.

Another consideration lies in the operation of the antenna. In general there are two modes to operate in: the far-field and the near-field. Compared with the far-field mode of operation, the near-field is a complicated area to understand. While there has been work done to characterize the near-field, problems that can be encountered are the stored energy of a signal and reactive power.⁴⁵ Thus, to avoid the complications inherent to operating in the near-field, this study conducted all of its theoretical and experimental work in the far-field. To operate in the far-field, certain criteria must be met which puts restrictions on minimum distances of operation based on operating wavelength and antenna dimensions. The criteria for far-field that were used for this study are defined by Stutzman⁴⁶ as

$$\begin{aligned}
 R &\gg \lambda \\
 R &\gg D_{dish} \\
 R &> \frac{2D_{dish}^2}{\lambda}
 \end{aligned}
 \tag{18}$$

One can see from these equations that depending on the setup a different criterion will dominate. Later in this study, it will be shown that the proof-of-concept experiment is dominated by the second condition, while the notional terahertz diagnostic instrument must satisfy the third condition.

2. Parabolic Reflector Antennas

Reflector antennas have been studied for many years. They are generally derived from the conic sections: circle, ellipse, parabola, hyperbola, and straight line. The first reflector antenna was a cylindrical parabolic reflector created by Heinrich Hertz in 1888. Antennas were first used for experiments, but then as use of technology in warfare increased, they were developed for radar and communications. Since the dawn of the space age, reflector antennas have made large jumps in terms of size, gain, and application in order to keep up with the demand to track and communicate with space vehicles. Today, some of the most prominent reflector antennas include the Arecibo 1000-ft spherical reflector, the ATS-6 unfurlable 30-ft reflector, and the famed Effelsberg 100-meter radio telescope which has a maximum realizable gain of 83 dB.⁴⁷ These antennas are pictured below in Figure 12. Seeing the capabilities of such reflector antennas, it was decided to use a parabolic reflector antenna in the design of the notional terahertz diagnostic instrument.

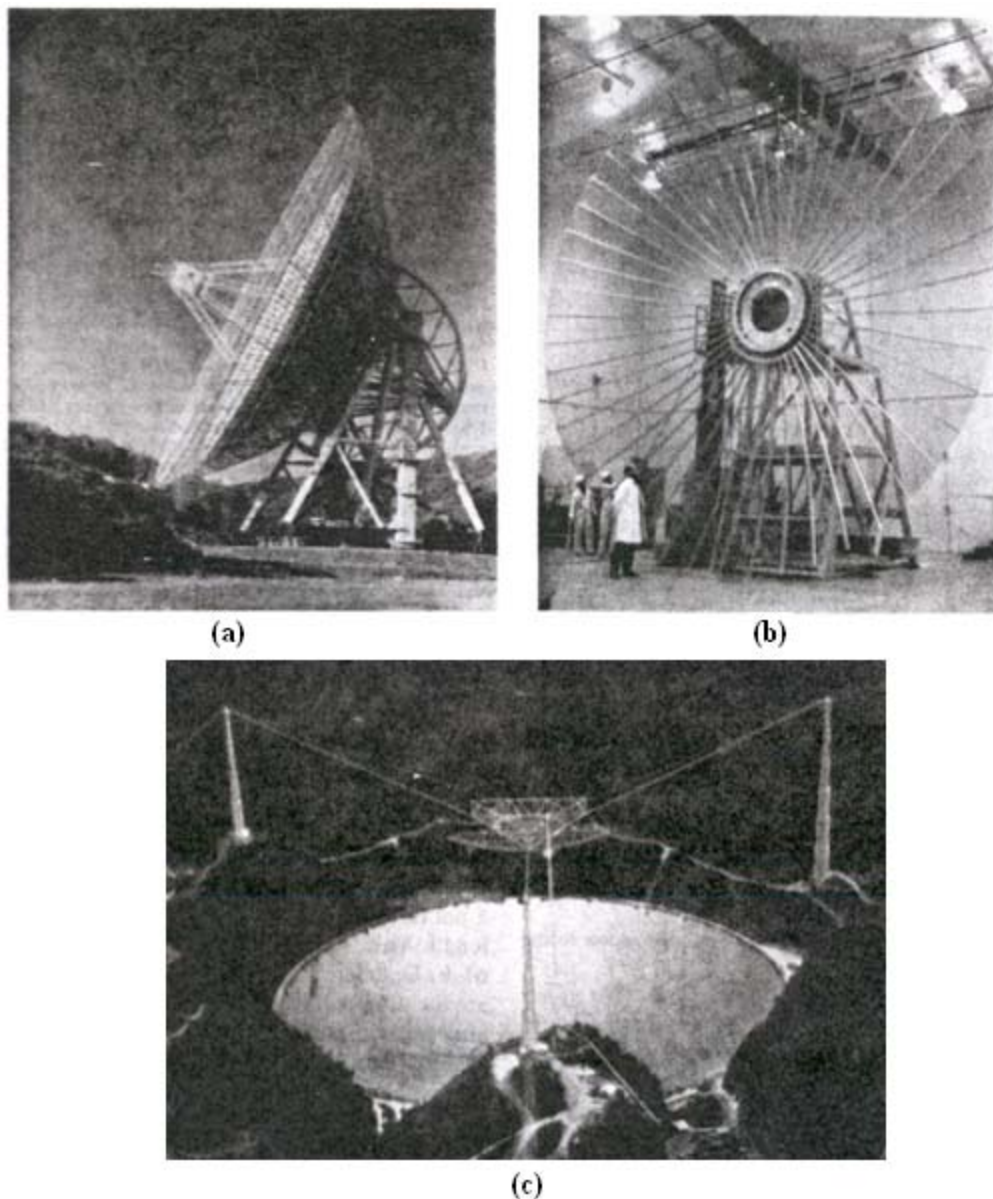


Figure 12: Several large reflector antennas (a) Effelsberg 100-meter radio telescope (b) ATS-6 unfurlable 300-ft reflector (c) Arecibo 1000-ft spherical reflector⁴⁷

In general, parabolic reflector antennas operate by using a smaller low gain antenna as a feed antenna which generates the signal inside the reflector. The emitted signal is then reflected off of the antenna dish and propagated outward from the antenna. The factor of most concern for application in the notional instrument is the antenna gain. Free space loss, as discussed previously, poses the largest threat to the operation of this system. If too much attenuation occurs on the way to and from the solid rocket exhaust plume, the scattering information will be lost in atmospheric noise and be useless in terms of

performing a diagnostic of the particles in the plume. The gain for a parabolic reflector can be calculated using the following equation.⁴⁸

$$G = \frac{4\pi}{\lambda^2} \left(\frac{\pi D_{dish}^2}{4} \right) \left\{ 6 \left[\frac{a_0 \gamma}{2} + \frac{a_2 \gamma^3}{4} + \frac{5}{12} a_4 \gamma^5 \right]^2 \right\} \quad (19)$$

The information inside the brackets is generally held as the gain factor of the antenna. For the purposes of designing the notional terahertz diagnostic instrument, a simplified version of this equation was used. It depends only on the diameter of the dish and the frequency of the transmitted light. It assumes a gain factor of 0.55 and is used in the development of the notional instrument for its ease of use.⁴⁹

$$G = 17.8 + 20 \log D_{dish} + 20 \log f \quad (20)$$

This equation combined with the restrictions for far-field operation set the basis for the design of the notional terahertz solid rocket exhaust plume diagnostic tool.

3. Horn Antennas

The proof-of-concept experiment was conducted in an indoor chamber that would not allow for the use of a parabolic antenna while satisfying the far-field criteria. Therefore, a different antenna type was selected: the horn antenna, which is a variety of aperture antenna. There are three types of rectangular horn antennas: (1) E-plane sectoral, which is flared only in the E-plane, (2) H-plane sectoral, which is flared only in the H-plane, and (3) a pyramidal horn, which is flared in both the E and H planes. The difference in the horn varieties can be seen in Figure 13.

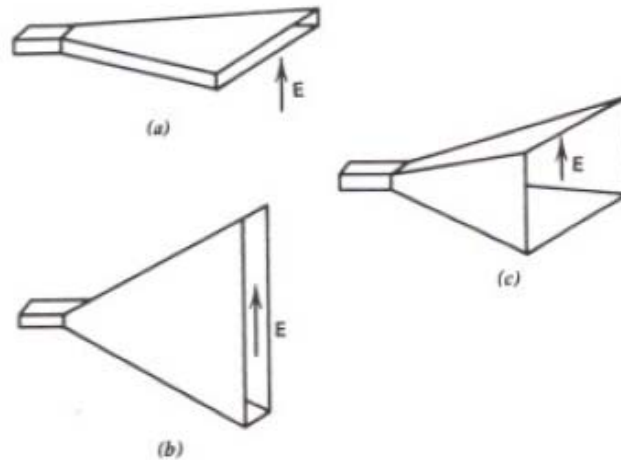


Figure 13: Horn antenna types: (a) H-plane sectoral (b) E-plane sectoral (c) Pyramidal⁵⁰

The proof of concept experiment utilizes only the pyramidal horn antenna, thus this section will only look at the theory for that specific type.

In general, a horn antenna provides a smooth transition for electromagnetic radiation from a waveguide into free space or vice versa. It operates in much the same manner as a megaphone amplifies the sound of someone's voice. Again, the important issue for this study is antenna gain. However, for the proof-of-concept experiment the size of the horn must also be taken into account so that the far-field criteria are not violated. Horn antennas are characterized by their H-plane and E-plane patterns which are derived from the antenna's gain. The gain can be calculated using the following equation assuming an aperture efficiency of 50%.⁵⁰

$$G = \frac{1}{2} \frac{4\pi}{\lambda^2} (AB) \quad (21)$$

In this equation A and B represent the horizontal and vertical dimensions of the aperture respectively. These two parameters are also used to determine the far-field restrictions that are placed on the experiment. The largest dimension of the horn antenna is the diagonal of the aperture which can be easily found using the horizontal and vertical dimensions. This dimension is then applied to the far-field criteria in Eq. (18) to determine the minimum distance for both the transmitter and the receiver.

C. Rayleigh Approach

The intensity of light scattered from a particle is a function of the incident intensity of light, particle radius, distance, and wavelength as shown in Eq. (15). Eq. (15) represents the total intensity of light scattered. In general, it is not feasible to collect all of the scattered light. In fact, only a small portion of this light can be measured through the collection aperture. In order to better analyze the situation, one can define a differential cross-section.

$$\frac{d\sigma_{ss}}{d\Omega} = \frac{9\pi^2 V^2}{\lambda^4} \left(\frac{m^2 - 1}{m^2 + 2} \right)^2 \sin^2 \phi \quad (22)$$

From Miles, Lempert, and Forkey⁴⁰, the total collected power becomes the integral of the number of particles multiplied by the scattering differential cross-section, the incident intensity, and the scattering efficiency over the collection solid angle. Namely,

$$P_{det} = \eta I_I N v \int_{\Omega_1}^{\Omega_2} \frac{d\sigma_{ss}}{d\Omega} d\Omega \quad (23)$$

The differential solid angle can be represented as

$$\delta\Omega = \sin(\phi) d\phi d\theta \quad (24)$$

which when applied to the integral for detected power becomes

$$P_{det} = \eta I_I N v \int_{\theta_1}^{\theta_2} \int_{\phi_1}^{\phi_2} \frac{9\pi^2 V^2}{\lambda^4} \left(\frac{m^2 - 1}{m^2 + 2} \right)^2 \sin^3(\phi) d\phi d\theta \quad (25)$$

Evaluating the integral in Eq. (25) for the power yields the equation

$$P_{det} = \eta I_I N v \frac{9\pi^2 V^2}{\lambda^4} \left(\frac{m^2 - 1}{m^2 + 2} \right)^2 \left(\frac{(\theta_1 - \theta_2)(\cos(3\phi_1) - \cos(3\phi_2) - \cos(9\phi_1) + \cos(9\phi_2))}{12} \right) \quad (26)$$

For a comparison between Mie theory and Rayleigh theory, Cox, DeWeerd, and Linden⁵¹ performed an experiment to measure the Mie and Rayleigh total scattering cross-section for several particles. The experiment used three different particle radii and a frequency sweeping source. They confirmed that while the criterion for Rayleigh scattering is met, the two theories produce the same results.

In a particular experimental setup, certain values can be controlled and are known. The values for incident intensity, wavelength, refractive index, and collection angle are generally known. The experiment will typically yield a value for the scattered power. Unfortunately, this leaves two unknown values and only one equation. Those values are particle number density and particle radius. In past experiments utilizing Rayleigh scattering, the number density was either known or reasonably approximated. For example, Zhang *et al*³⁵ measured the size and number density of glycogen molecules. However, in their experiment, the size of glycogen was relatively well known as well as the concentrations of the solutions they used which gives a relation to number density. Also, An-Le *et al*³⁰ measured the size of argon clusters using Rayleigh scattering. However, they were able to relate both size and number to their reservoir pressure. Unfortunately, these values are not generally known for alumina particles in solid rocket plumes. There have been studies conducted to determine particle size based on the propellant characteristics. O. B. Kovalev⁵² discussed the formation of aluminum oxide in rocket plumes and generated an analytical prediction method for the size of the particles. However, the particle number density and size in a typical

rocket plume is generally unknown. Therefore, this technique may be restricted to measuring the product of NV^2 unless other methods can be developed in the future. One method would involve sweeping frequencies. This technique would start at the smallest frequency in the terahertz regime and increase by discrete amounts. This increase would remove the scattering signal from the larger particles because they would no longer satisfy the Rayleigh criterion. These particles would be in the Mie regime where the off incident direction scattering is negligible. The change in scattered signal return can be measured and analyzed to calculate a number density for a certain group of particle radii. The process could be repeated to account for all particle sizes of interest. Also, using interferometry could lead to measuring the particle velocity.⁵³

In order to calculate the actual power received from a scattering center, the transmission losses and gains from antennas must be taken into account. Friis transmission formula is used to determine the power received based on the space loss from Eq. (17) and the gains of the antenna.

$$\frac{P_r}{P_t} = G_t \left(\frac{\lambda}{4\pi R} \right)^2 \quad (27)$$

Using this formula with Eq. (25), the power ratio for an actual setup can be written as

$$\frac{P_r}{P_t} = G_t G_r \left(\frac{\lambda}{4\pi R} \right)^2 \eta N_v \frac{9\pi^2 V^2}{A\lambda^4} \left(\frac{m^2 - 1}{m^2 + 2} \right)^2 \int_{\theta_1}^{\theta_2} \int_{\phi_1}^{\phi_2} \sin^3(\phi) d\phi d\theta \quad (28)$$

CHAPTER 6

EXPERIMENTAL SETUP AND PREDICTED RESULTS

A. Experimental Setup

The proof-of-concept experiment was designed to be a scaled version of the notional terahertz diagnostic instrument working with typical solid particles in a solid rocket plume. Therefore, the sphere sizes were scaled with the experimental wavelength (12.24 cm) in order to meet the Rayleigh scattering criterion, reproducing the plume environment as far as particle size to wavelength ratio is concerned. The Electrical and Computer Engineering Department at the University of Colorado at Colorado Springs is currently developing the terahertz source that will eventually be used in this project. This source is designed to operate at 300 GHz with an output power of 1 kW with minimal frequency sweeping capabilities. Assuming that the notional terahertz diagnostic instrument would have a non-frequency sweeping source, the wavelength of 1 mm would dictate a maximum particle radius of 100 microns in order to stay within Rayleigh theory constraints. The proof-of-concept experiment utilized microwaves at a frequency of 2.45 GHz and wavelength of 12.24 cm. This source had a fixed frequency which set the maximum particle radii at 12.24 mm. The experiment looked at particles whose radius ranged from 4.76 mm to 9.53 mm.

All of the experiments were conducted inside a microwave anechoic chamber at the University of Colorado at Colorado Springs. The setup consisted of a power source transmitted through a horn antenna. The scattered energy from the particle was collected in a second horn antenna. The power source used in the experiment is a National Electronics 2 kW magnetron source which was coupled with a National Electronics Isolator, a waveguide measurement piece, and an Agilent Tuner. The power source along with attached horn antenna can be seen in Figure 14.

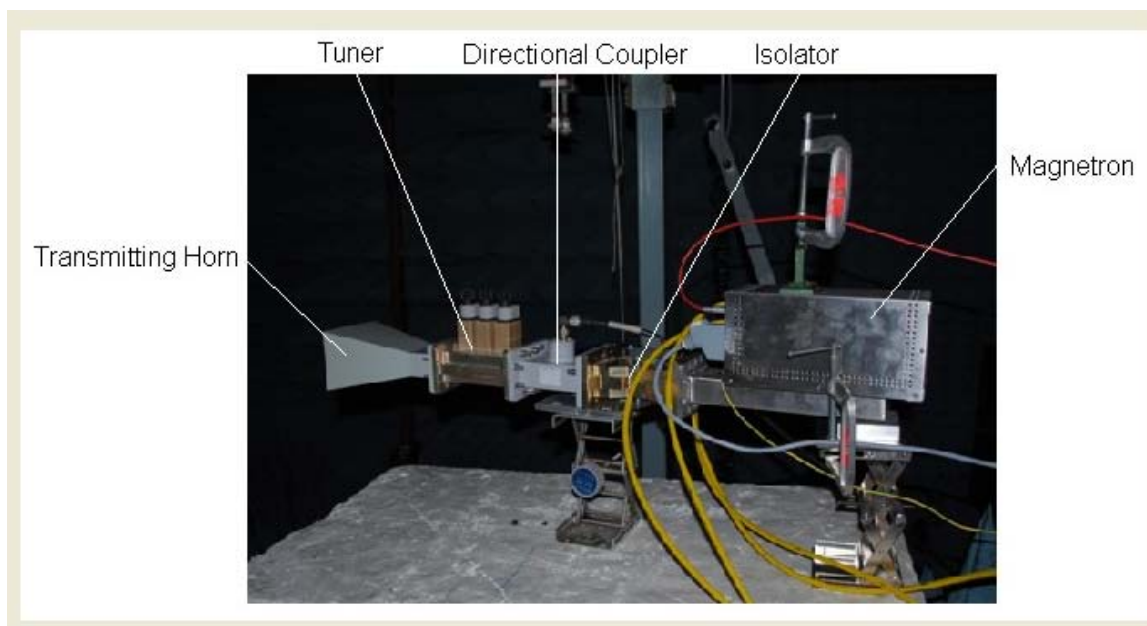


Figure 14: 2 kW magnetron source and horn antenna

The forward power from the 2 kW magnetron source was measured using a HP power sensor connected to an Agilent power meter. The measured data was recorded using Lab View 8.2.1. Microwaves were passed through coaxial cables and emitted into the anechoic chamber from a 10 dB standard gain horn. The microwaves traveled approximately 2.44 m to the sphere as shown in Figure 15 satisfying the far-field requirement defined by Eq. (18).



Figure 15: Distance traveled by microwaves from transmitter

The spheres were made out of three different materials: 2017-T4 aluminum, brass, and stainless steel 302. The spheres had several different radii which are 9.53 mm, 7.94 mm, 6.35 mm, and 4.76 mm. They were supported with 6.35 mm outer diameter (4 mm inner diameter) quartz tubes that were approximately 14 cm apart for the double sphere setup. The 4.76 mm radius aluminum spheres can be seen on the quartz support tubes in Figure 16 in both a single and a double sphere setup.

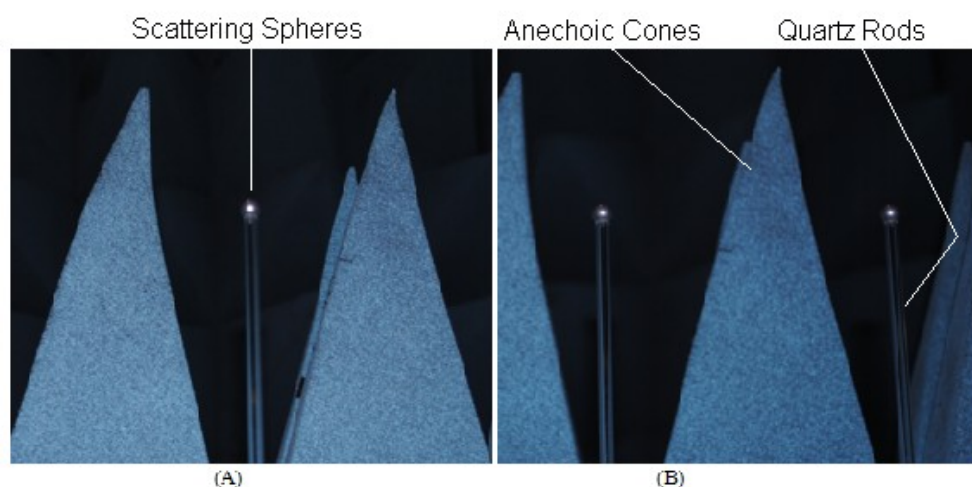


Figure 16: Sphere configuration (A) Single and (B) Double

The scattered microwaves were collected in a 14.7 dB standard gain horn. The received power was passed through coaxial cables out the anechoic chamber to an HP power sensor which was connected to the Agilent power meter. The receiving horn can be seen in Figure 17 connected to the power sensor. Figure 18 and Figure 19 show the entire setup from the perspective of the spheres and an observer. Figure 20 provides a general overhead view of the experimental setup.

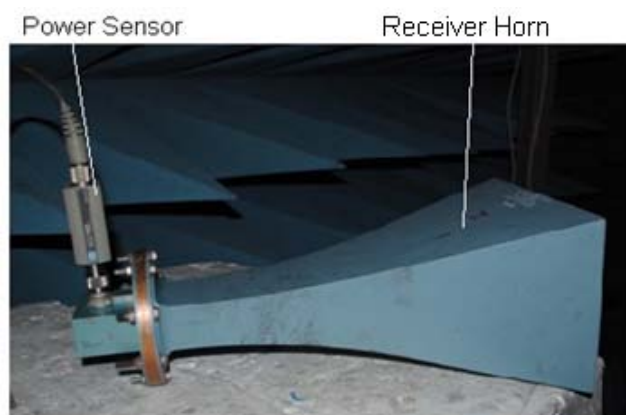


Figure 17: Receiving horn for scattered microwaves



Figure 18: Experimental setup from observer perspective



Figure 19: Experimental setup from sphere perspective

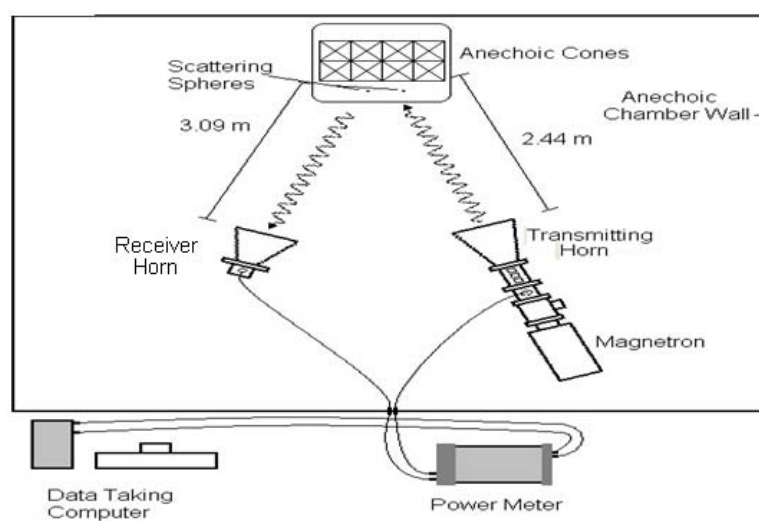


Figure 20: Overhead view of experimental setup

The concept of using microwave horns as both the transmitting and receiving antennas is consistent with Zhang, Shneider, and Miles³⁸ who used a similar setup to measure Rayleigh scattering using microwaves from resonance-enhanced multiphoton ionization in argon. They used a 10 mW source at a frequency of 12.6 GHz and collected the scattered signal in a microwave homodyne receiving system. Shneider and Miles³⁶ also performed microwave Rayleigh scattering. Using frequencies of 3 and 6 GHz, they performed plasma diagnostics by treating the plasma as a point dipole source and collecting the Rayleigh scattered light from the plasma.

The experiments performed in this study were repeated for each of the sphere sizes and materials. The input power from the microwave source ranged from approximately 200 Watts to 2000 Watts. The experiment was also run with only the quartz rod in the chamber. The collected power from the “no sphere” run was subtracted from each of the recorded tests with a sphere in the chamber as a zero signal reference. The difference was taken as the scattered power and was used in comparison with the other tests. Eight data points were taken which represent the average of multiple individual tests. The eight points corresponded to input powers that are approximately 200 Watts to 2000 Watts with a 200 Watt interval.

B. Predicted Experimental Results

The aforementioned proof-of-concept experimental setup parameters were input into a MATLAB code in order to generate predicted results for the tests conducted. The known parameters for the proof-of-concept experiment include the gains of the horn antennas, the geometry of the experiment, and the free space loss for transmission. The linear gain for the transmitting and receiving antennas were measured to be 10 and 29.51 respectively. The free space loss for the transmission of the input power is 1.59×10^{-5} . The geometry determines the bounds of the integral term from Eq. (28) which yields a value of 0.021. Inputting these parameters into Eq. (28), it can be simplified to

$$\frac{P_r}{P_t} = 18.7989 \eta N v r^4 \left(\frac{m^2 - 1}{m^2 + 2} \right)^2 \quad (29)$$

Eq. (29) provides the basis for the Matlab code which can be seen in Appendix B.

The two unknown material properties in Eq. (29) are the index of refraction and the scattering efficiency. Reference 54 investigated values for the index of refraction based on different wavelengths of

light for aluminum. Figure 21 shows the results for the relation between wavelength and index of refraction. It is obvious that as wavelength continues to increase the index of refraction also continues to increase.

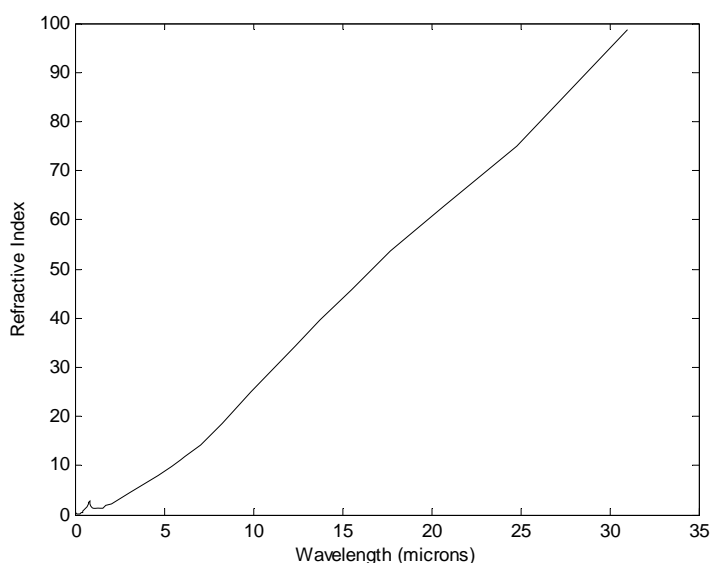


Figure 21: Relation between refractive index and wavelength for aluminum

The relation in Figure 21 agrees with Reference 55 which states that as the frequency decreases, the index of refraction for metals increases to infinity. Figure 22 and Figure 23 show the expected trends for the proof-of-concept experiment. In general, the index of refraction at microwave and terahertz frequencies for various materials is unknown. A thorough review of the existing literature yielded no conclusive results. Therefore, an assumed index of refraction of 2 and a scattering efficiency of 100% were used in Figure 22 and Figure 23 so that general trends can be seen. Figure 22 shows the linear trend from Eq. (29) between the source power and the scattered power as well as the increase in scattered power associated with an increase in the number of scattering centers for a sphere with a radius of 9.53 mm. Figure 23 depicts the fourth order relationship between the radius of the scattering sphere and the scattered power as defined by Eq. (29). Figure 24 highlights the role that the index of refraction plays in the scattered power collected from a sphere with a radius of 9.53 mm and a scattering efficiency of 100%. It is clear that the scattered power is not substantially affected by the index of refraction.

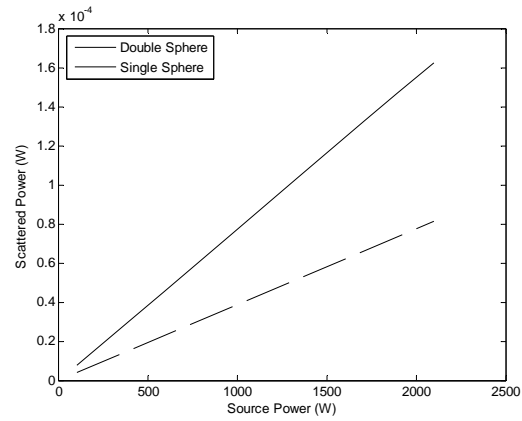


Figure 22: Scattered power versus source power for generic sphere with $r = 9.53$ mm and $m = 2$

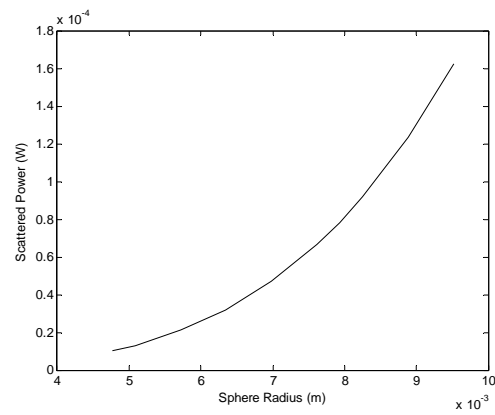


Figure 23: Scattered power versus sphere radius with $m = 2$

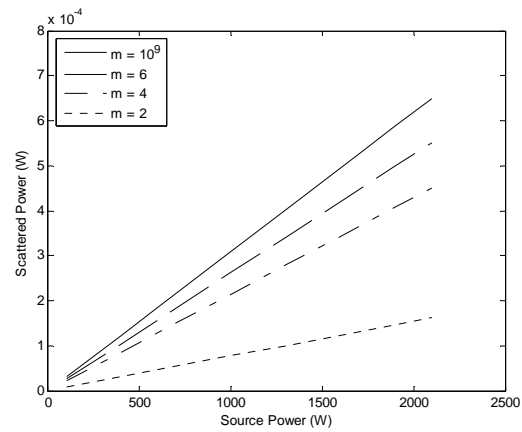


Figure 24: Scattered power versus source power for a 9.53 mm radius sphere as a function of the refractive index

The effect of the scattering efficiency must also be taken into account for the experiment since it is also not generally known at the wavelengths of interest in this study. While Figure 24 shows that an increase in the refractive index leads to an increase in the scattered power, this increase can be offset by a decrease in the scattering efficiency of a particle. Figure 25 shows this phenomenon by holding the index of refraction fixed at 10^9 and varying the scattering efficiency.

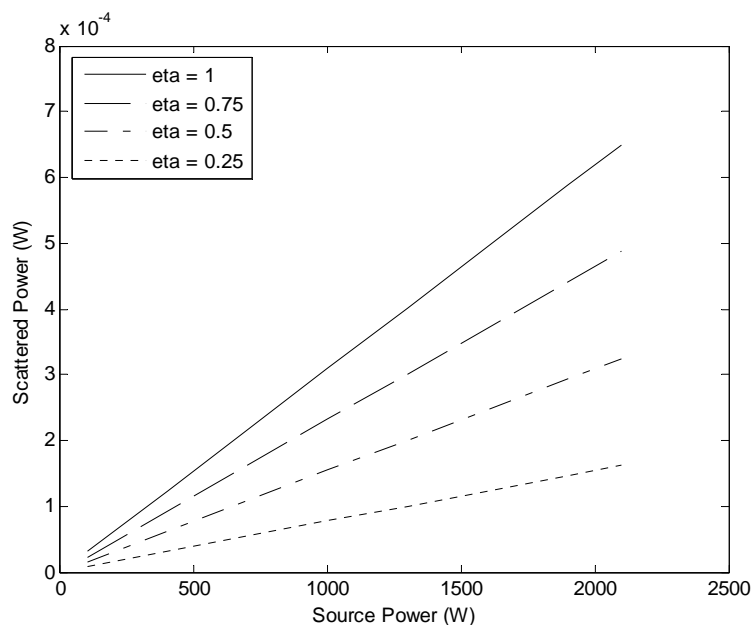


Figure 25: Scattered power versus source power for a fixed refractive index of $m = 10^9$

CHAPTER 7

RESULTS AND DISCUSSION OF PROOF OF CONCEPT EXPERIMENT

A. Single Sphere Results

The first tests done for the proof-of-concept used only a single sphere as the scattering center. Only two materials were used for these tests: aluminum and brass. The results for these tests can be seen in Figure 26 and Figure 27.

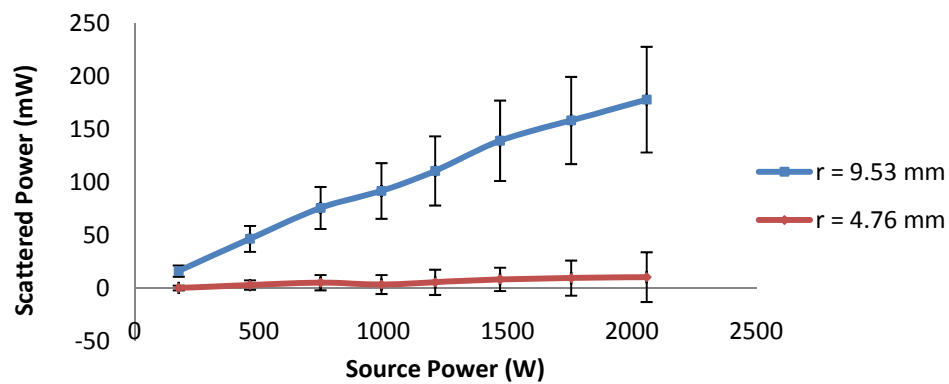


Figure 26: Scattered power versus source power for one aluminum sphere

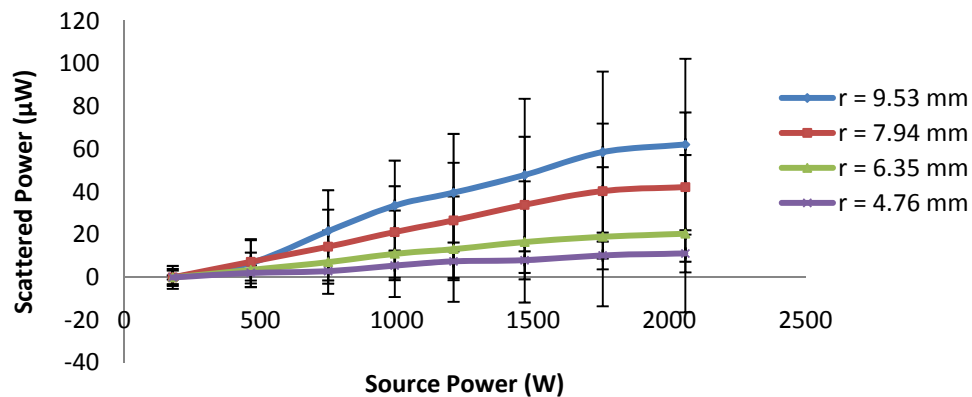


Figure 27: Scattered power versus source power for one brass sphere

In Figure 26 and Figure 27, the linear trend, as defined by Eq. (29), is apparent. However, the error bars for the measurements are very large. The error stems from the small signal to noise ratio encountered in these tests. In Figure 26, the average signal to noise ratio is 1.06 for the 9.53 mm radius

sphere and 1.004 for the 4.76 mm radius sphere. In Figure 27, the signal to noise ratio ranges from 1.005 to 1.031. For accurate measurements, a larger signal to noise ratio is needed. In order to improve the signal to noise ratio, the remainder of the tests used two spheres which acts to approximately double the scattered signal according to Eq. (29).

B. Double Sphere Results

The next set of tests were conducted with two spheres for reasons mentioned above. Each test data point was repeated five times and the average of these tests is reported. The error bars on the graphs represent the standard deviation for the group of tests. Each different material and sphere size was used in these tests. The results for these runs can be seen in Figure 28, Figure 29, and Figure 30.

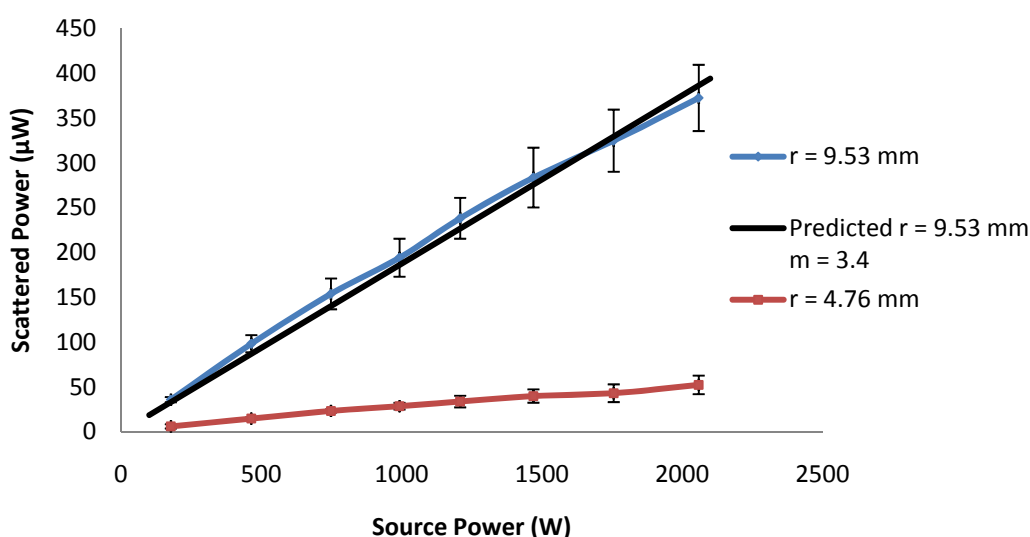


Figure 28: Scattered power versus source power for two aluminum spheres

The predicted line in Figure 28 was generated using Eq. (29) and assumed values for the unknown index of refraction and scattering efficiency. The scattering efficiency was assumed to be 100%, and an index of refraction of 3.4 provided the best fit to the experimental results for the 9.53 mm radius sphere. Similarly, values for the index of refraction were chosen to produce best fit prediction lines for Figure 29 and Figure 30. The value for brass is 6.0, and the value for stainless steel is 1.85. While the true values remain unknown, the determination of these parameters is beyond the scope of this study. However, for a terahertz diagnostic instrument, the actual values for alumina will need to be determined for the operating wavelengths and temperatures.

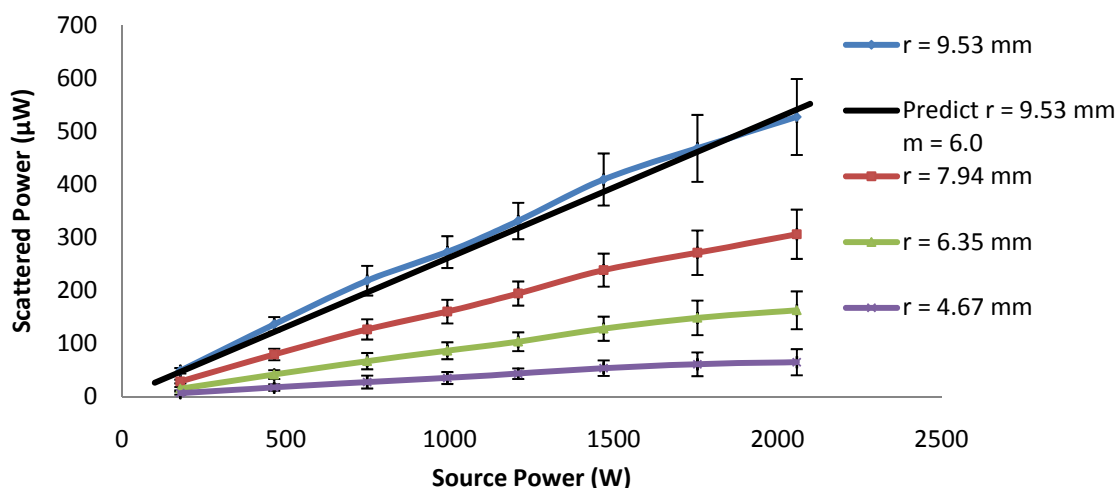


Figure 29: Scattered power versus source power for two brass spheres

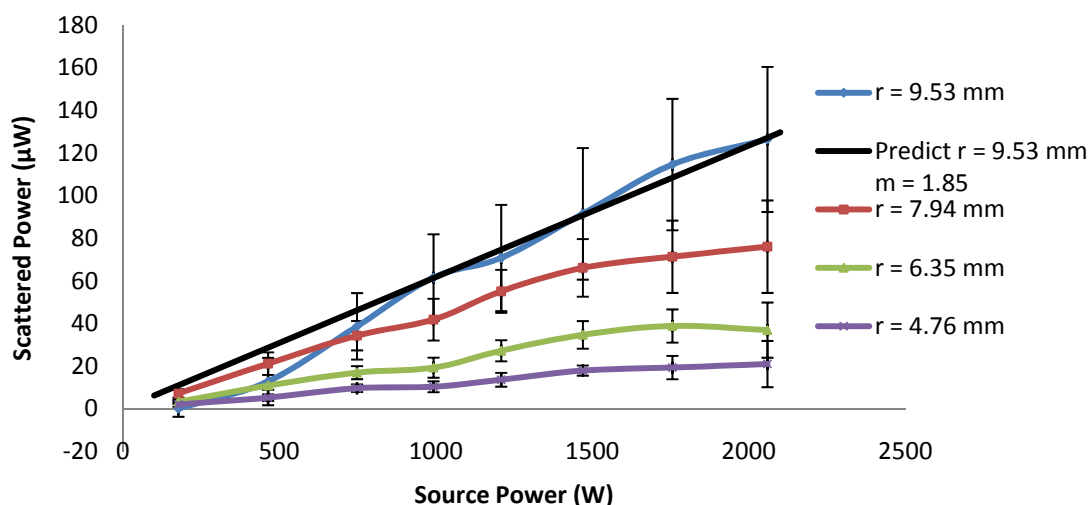


Figure 30: Scattered power versus source power for two stainless steel spheres

In each of the tests there is a linear trend for the experiment, which is expected based on Eq. (29). Comparing these figures to that of the single sphere data, one can clearly see the increase in the scattered signal along with the decrease in the error bars. The signal to ratio for these tests, however, is still low ranging from 1.009 to 1.197. While it may be the case for each of the materials in the experiment that the index of refraction is much higher than the assumed value, the scattering efficiency can offset the increase in scattered power. Using 10^9 as the refractive index for each material, a scattering efficiency of 60.65% for aluminum would create the same predicted trend shown in the results based on Eq. (29). Likewise, a scattering efficiency of 84.83% readjusts the brass predicted trend, and an efficiency of 19.96% for

stainless steel satisfies the trend difference. The reality for the materials is probably a compromise between these two values in order to generate the results from the proof-of-concept experiment. It is obvious that for any experiment or diagnostic, accurate values for these parameters are necessary.

C. Sphere Number Comparison

Figure 31 shows the ratio of the scattered power between two spheres and a single sphere for the 9.53 mm radius sphere of aluminum.

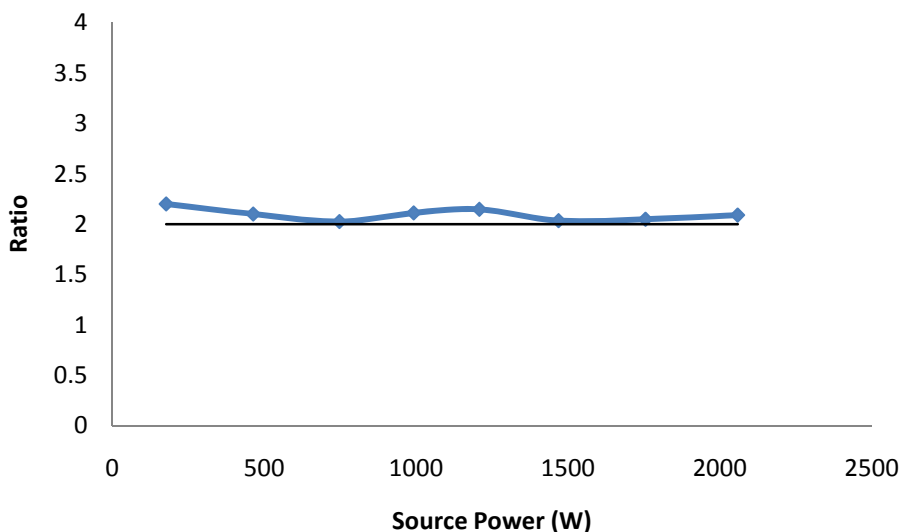


Figure 31: Aluminum sphere number comparison

In Figure 31, the highest returned scattered power for the double sphere set up is 372.6 μW , and the single sphere setup maximum is 178.3 μW . Within the errors bars of the two different setups, there is a factor of two increase in the scattered power as expected by Eq. (29); therefore, doubling the scattering centers leads to an effective doubling of the collected Rayleigh scattered signal. The low signal to noise ratio is the source of the fluctuations above the ratio of 2.

D. Sphere Size Comparison

The next comparison for the collected data was between the different sphere sizes. According to Eq. (29) the relation between the different sphere radii should be fourth order. Thus for Figure 32, Figure 33, and Figure 34 the different sphere sizes were compared within the same material. For each of the graphs, the highest output power from the source was used in order to get the highest signal to noise ratio. Also, only the double sphere data was used in creating the following figures.

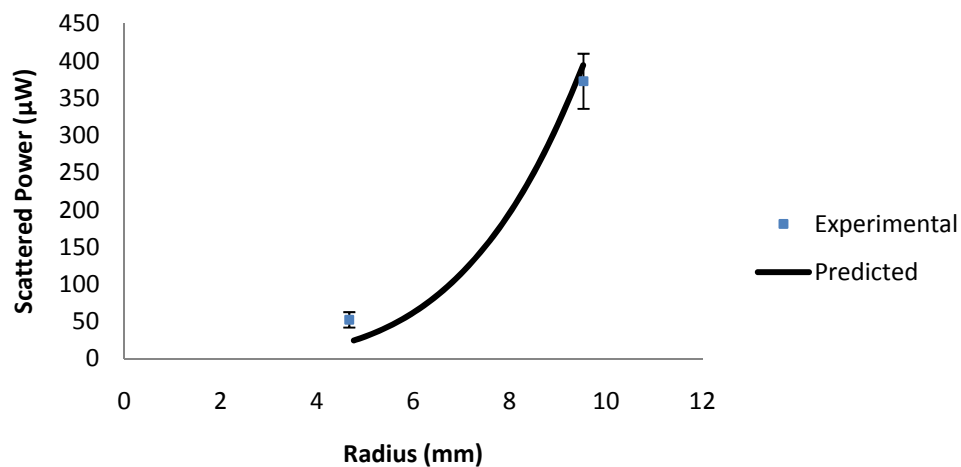


Figure 32: Aluminum sphere size comparison

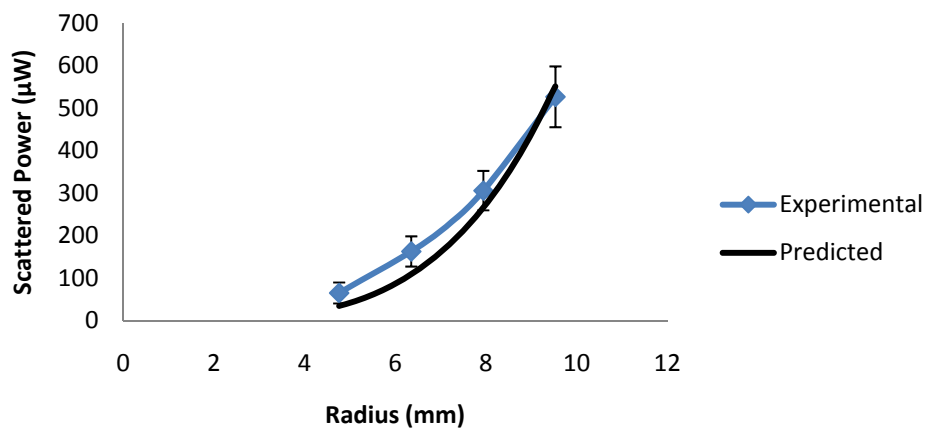


Figure 33: Brass sphere size comparison

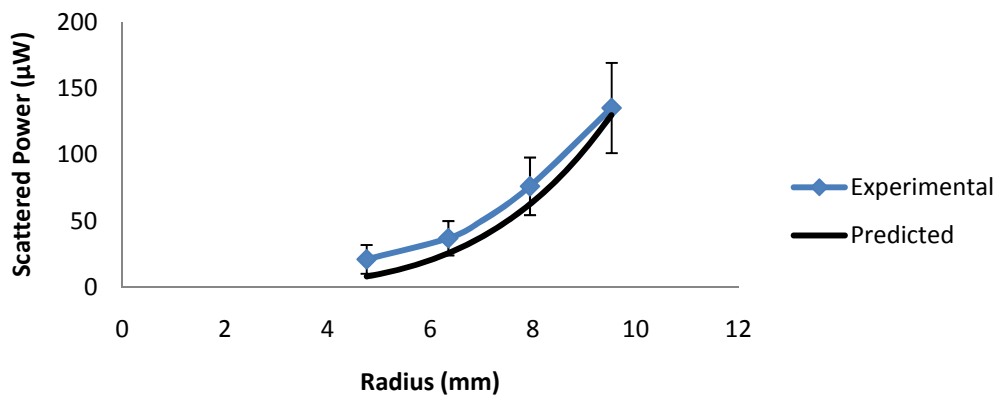


Figure 34: Stainless Steel sphere size comparison

In Figure 32, Figure 33, and Figure 34, the fourth order relation between radius and scattered power agrees with Eq. (29). The predicted line in these figures was generated using the best fit index of refraction found earlier in this chapter. Those values are 3.4, 6.0, and 1.85 for aluminum, brass, and stainless steel respectively. The largest sphere radius was used to determine the best fit index of refraction because it yielded the highest signal to noise ratio and, therefore, accuracy. However, the fit for the largest sphere radius is not perfect, and was modified in order to improve the fit for the smaller radii. It can also be seen that even with a modified index of refraction the theory and experiment are not a perfect match especially at smaller sphere radii. The discrepancy may be due to uncertainties in the index of refraction as well as in the scattering efficiency. Also, the small signal to noise ratio is still a factor in the experimental error.

E. Sphere Material Comparison

The final comparison for the data from the proof-of-concept scattering experiment was between the three different sphere materials. The difference between the materials should be based solely on the difference in the index of refraction and scattering efficiencies between the different materials. Figure 35 and Figure 36 show the scattered power versus source power curves for the sphere sizes of 9.53 mm and 4.76 mm.

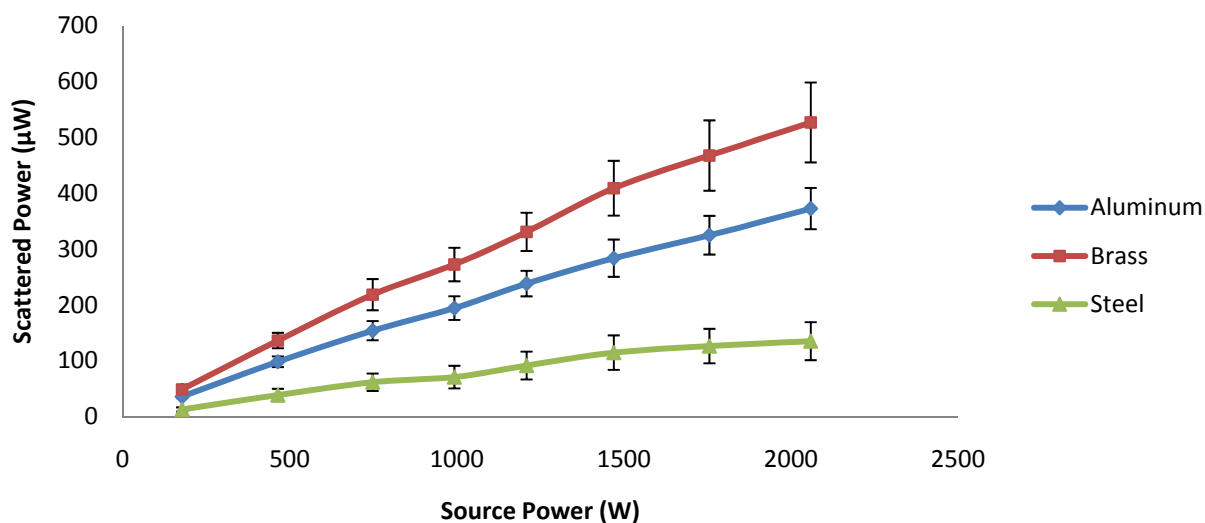


Figure 35: Sphere material comparison for 9.53 mm radius sphere

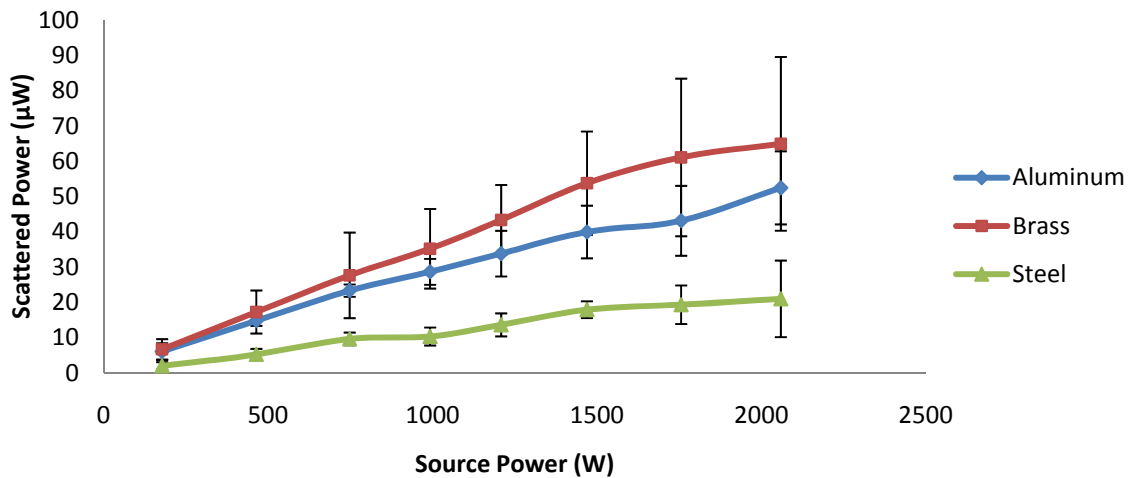


Figure 36: Sphere material comparison for 4.76 mm radius sphere

It can be seen in Figure 35 and Figure 36 that the index of refraction and the scattering efficiency directly affect the returned scattered power as Eq. (29) indicates.

F. Experiment Discussion

The results of the proof-of-concept experiment show that Rayleigh scattering can be used to determine particle size when the number density of the particles is known. The data is in good agreement with the trends set forth by the theoretical calculations for the experiment. However, there are some differences between theory and experiment and sources of error that need to be addressed.

1. Sources of Error

There were several sources of error that arose during the process of conducting the proof-of-concept experiment. One of the most prominent sources of error between the theory and the experiment was the small signal to noise ratios generated during the tests. The maximum ratio from the tests was 1.18 which is well below the threshold for accurate data. The low ratio led to large error bars in the experiments. The large amount of noise was mostly generated by reflection inside the anechoic chamber. The reflection led to milli-Watts of measured power for the zero traces of the experiment. Another large source of error was the uncertainty in the index of refraction at microwave frequencies and the scattering efficiency of the materials used in the experiment. These parameters have a strong influence on the predicted amount of scattered power for each of the tests.

Other sources of error include the power sensors used to measure both the transmitted and scattered signals. These sensors have a quoted measurement noise of $<110\text{nW}$ which is 0.16% of the lowest measured signal. Another factor would be minor fluctuations in the transmitted signal. For the purposes of ease of measurement, the magnetron source was allowed to fluctuate by $\pm 0.64\text{ W}$. Any movement of the anechoic cones in the chamber could also have an effect on the consistency between different test runs. Another experimental setup factor that would play into the error bars is the quartz rods. While mostly microwave transparent, they still contributed slightly to the measured powers. Again if the rods' position is moved slightly the reflected signal could change leading to inconsistencies between the individual runs. Finally, any discrepancies on the spheres themselves would lead to a change in signal based on their orientation on the quartz rods. The spheres were not perfectly spherical, and they were not set on the rods the same every time.

2. *Differences Between Theory and Results*

The main difference between theory and results was in the magnitude of the returned scattered power. The experimental values for scattered power were only slightly different than the predicted results for the larger sphere radii. However, the percent differences grew for the smaller sphere radii. Table 5 shows the percent difference between the predicted results and the experimental data for the double sphere tests.

Refractive Index		% Difference
3.40	9.53 mm Al	-5.45
	4.76 mm Al	113.12
6.00	9.53 mm Br	-4.40
	7.94 mm Br	15.06
	6.35 mm Br	49.44
	4.76 mm Br	88.11
1.85	9.53 mm St	4.18
	7.94 mm St	21.50
	6.35 mm St	44.13
	4.76 mm St	159.06

Table 5: Differences between predicted and experimental results

It is important to note again that the scattering efficiency for the indices of refraction was assumed to be 100%. It is most likely a tradeoff between the actual index of refraction with a lower scattering efficiency. The increase in percent difference as the sphere size decreases is most likely a result of the uncertainty in this trade off and the low signal to noise ratio that occurs at the smaller radii. Despite these differences, the experimental results still show the capability of calculating the particle radius based on the scattered data. It is clear that each of the sphere materials and sizes had a unique scattered power which would enable identifying a particle based on its scattered signal.

CHAPTER 8

DEVELOPMENT OF NOTIONAL TERAHERTZ INSTRUMENT

A. Notional Terahertz Instrument

The proof-of-concept experiment demonstrated the capability of measuring particle size based on the amount of scattered light received if the number density of the particles is known. In order to extend the principles explored in the experiment to the diagnostic of a solid rocket exhaust plume, the Rayleigh theory and far-field criteria must be revisited.

For an actual experimental setup involving terahertz radiation and Rayleigh scattering, one must consider the challenges of transmitting across large distances while scattering off particles inside the rocket plume. For the predictions of the required power from a source, certain assumptions were made. For Rayleigh theory to apply, the wavelength was ten times greater than the particle radius. Also, the criteria for far-field transmission were used as defined in Eq. (18) by Stutzman.⁴⁶ After satisfying these criteria, the Friis transmission formula⁴² from Eq. (27) was used to calculate the ratio between the power at the scattering particle and the power transmitted. The notional setup uses parabolic antennas to transmit and receive. The gains for the antennas are based on frequency and the radius of the dish and can be calculated with Eq. (20).⁴⁹ With this setup, the integral bounds of the scattering cross-section can be defined in terms of the distance to the particle and the radius of the antenna dish; namely,

$$\phi_1 = \frac{\pi}{2} - \tan^{-1}\left(\frac{r_{dish}}{R}\right) \quad \phi_2 = \frac{\pi}{2} + \tan^{-1}\left(\frac{r_{dish}}{R}\right) \quad (30)$$

$$\theta_1 = \frac{\pi}{4} - \tan^{-1}\left(\frac{r_{dish}}{R}\right) \quad \theta_2 = \frac{\pi}{4} + \tan^{-1}\left(\frac{r_{dish}}{R}\right) \quad (31)$$

The final ratio between received power and transmitted power can be written as

$$\frac{P_r}{P_t} = G_t G_r \left(\frac{\lambda}{4\pi R}\right)^2 \eta N v \frac{9\pi^2 V^2}{A\lambda^4} \left(\frac{n^2 - 1}{n^2 + 2}\right)^2 \int_{\theta_1}^{\theta_2} \int_{\phi_1}^{\phi_2} \sin^3(\phi) d\phi d\theta \quad (32)$$

Figure 37 shows the effects of distance and antenna size on the power ratio Eq. (32) for a single 100 micron scattering particle. The graphs show that the while a large antenna provides more gain, the effects of increased distance, due to the far-field restrictions, are a greater detriment to the power ratio.

Overall, the relation is inversely proportional to the fourth power of the range. Figure 38 shows the relation between antenna radius and the power ratio assuming that the range is at the minimum distance while still satisfying the far-field criteria. Again it shows the inverse proportionality to the fourth power of the distance to the particle. The Matlab code used to generate these plots can be seen in Appendix C.

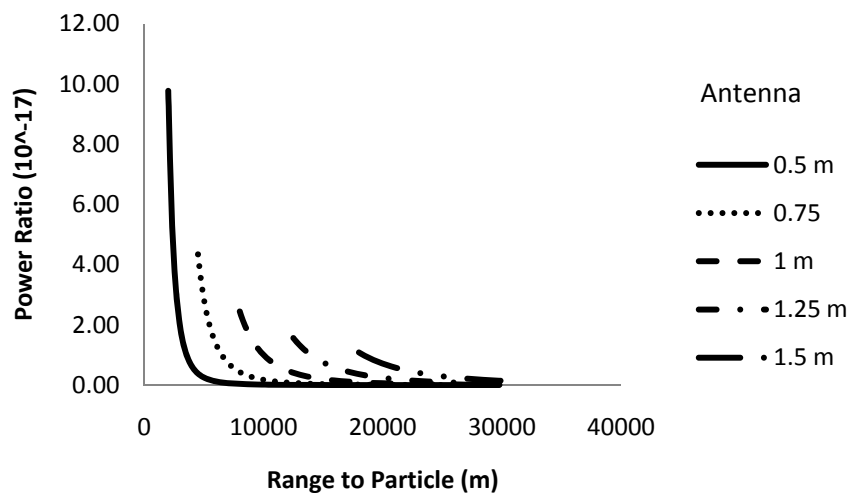


Figure 37: Relation between range to particle and power ratio with multiple antenna radii

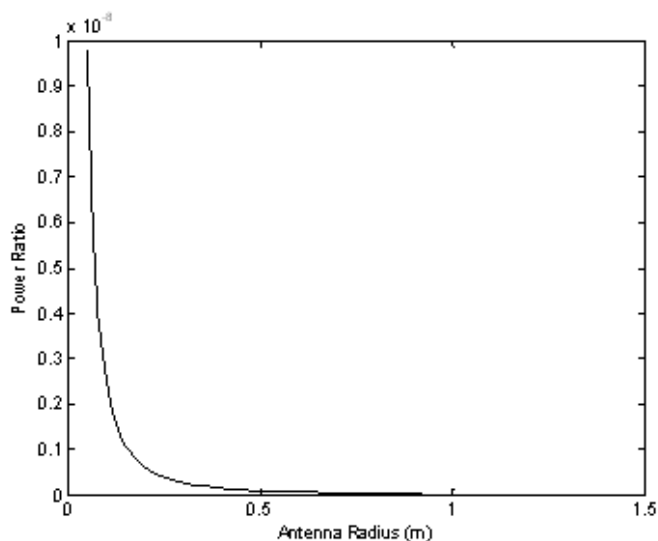


Figure 38: Relation between antenna radius and power ratio assuming minimum range to particle

From Figure 37 and Figure 38, one can see that, for a notional terahertz diagnostic instrument, a high power source is required with high gain antennas. These figures show that the biggest detriment to

scattered power is distance. Also, the power ratio for a single particle is very small. However, the number density for solid rocket plumes can be calculated for a Castor 120 solid rocket motor to be on the order of 10^8 to 10^{10} particles per cubic meter using a mass flow of 3.54 kg/s and a particle mass percentage of 32%.⁵⁶ This number density would allow a 1 kW source using 1.5 m radius antennas to measure scattered powers in the μW range at a distance of 20 km. Figure 39 depicts what the notional setup may look like.

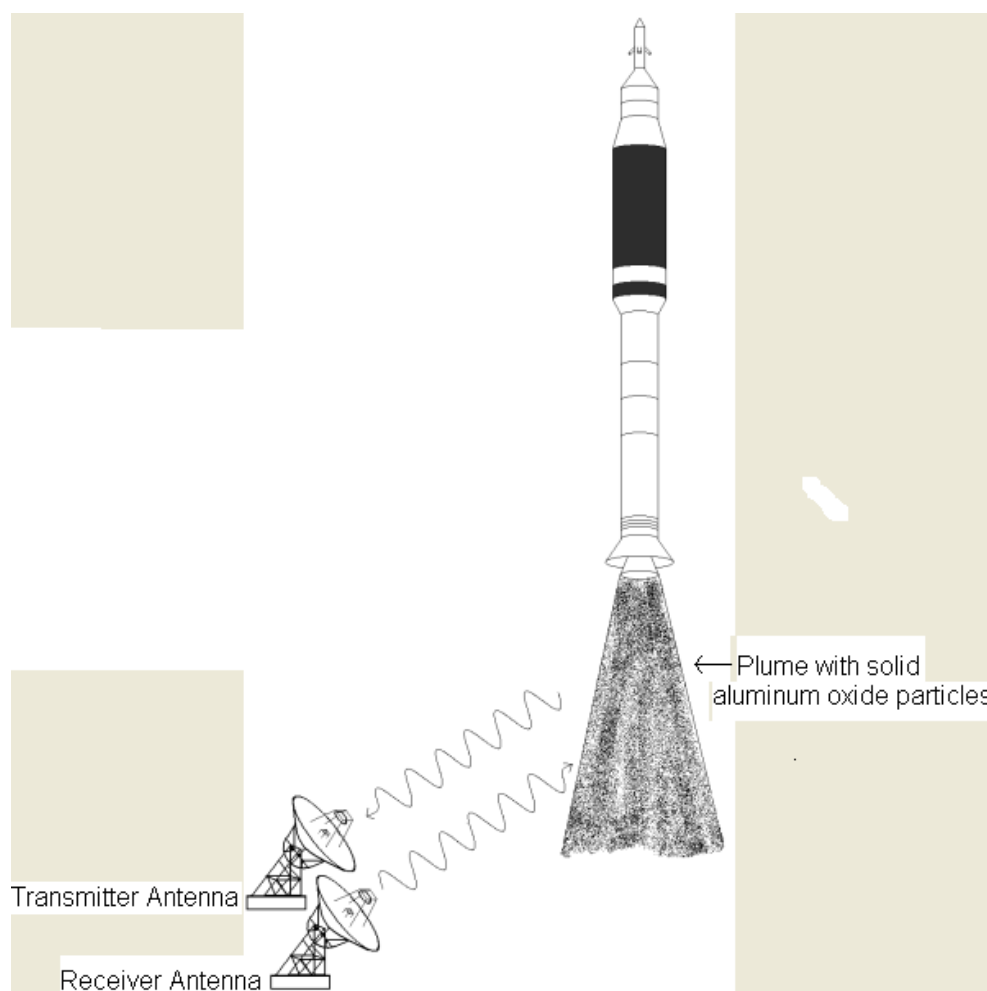


Figure 39: Notional terahertz diagnostic instrument

B. Complications of Implementation for Notional Terahertz Instrument

The two largest complications arising for the implementation of the notional terahertz diagnostic instrument are the power source and the antenna. As discussed in Chapter 2, there is a current lack of high power sources that operate in the terahertz regime. While the 1 kW source that was also previously discussed would prove beneficial to the terahertz diagnostic tool, it still would only be able to generate

microwatts of scattered power at a range of 20 km. This power could easily be lost in some atmospheric disturbance or in transmission or receiving inefficiencies. Thus, for a very versatile source, the output power should be in the MW range. Also, the proposed source lacks one capability that would be necessary for a single source instrument to be able to interrogate the plume of a solid rocket motor. That capability is the ability to frequency sweep across the terahertz regime. Frequency sweeping is needed to solve the single Rayleigh theory equation with the two unknowns of particle radius and number density as described in Ch. 5 Sec. C. Without this capability, several sources would be needed to conduct an accurate diagnostic. The source is only one issue for the instrument; an antenna would still need to be developed in order to make use of the source. At a range of 20 km the antenna could be 3 m in diameter. While not the largest antenna by any measure, it is still a sizeable undertaking. The antenna setup would also need the ability to track the trajectory of the rocket in order to provide continuous data on the rocket plume characteristics. Also, the design for the notional terahertz instrument relied heavily on a high gain to be realized by the antenna. The transmission efficiencies of the antenna and the feed antenna would need to be adequate in order to generate the necessary gain.

Another problem with using an actual terahertz instrument would be the atmospheric conditions on the day of use. Terahertz radiation is easily absorbed by water. Thus, an excess of moisture would largely hinder the operation of the terahertz instrument. Figure 40 below shows the attenuation effects of several different weather conditions.⁴⁴

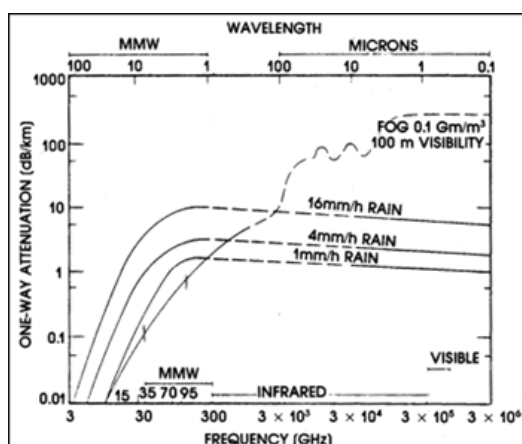


Figure 40: Attenuation due to water for terahertz instrument⁴⁴

It is important to note that the y-axis is attenuation per km. This means that on a foggy day the one-way loss for the terahertz instrument would be about 20 dB. This would absolutely destroy any chance of performing any accurate measurements.

The last major problem that would have to be addressed prior to conducting actual real-time diagnostics is the inter-particle interactions. During the tests of the proof-of-concept experiment, there were instances when adding more scattering centers produced the appropriate increase in measured scattered power. The following figures are from an earlier setup of the experiment in which the receiving horn only had a 10 dB gain instead of the 14.7 dB gain horn used for the other runs. Figure 41, Figure 42, and Figure 43 show the effects of adding more scattering centers. The spheres used were the 9.53 mm and 4.76 mm radii aluminum spheres. The triple sphere setup is similar to the setup seen in Figure 16. The three spheres were placed approximately 14 cm apart. The spheres were in a line perpendicular to the direct line of sight of the transmitting antenna as in the two sphere setup.

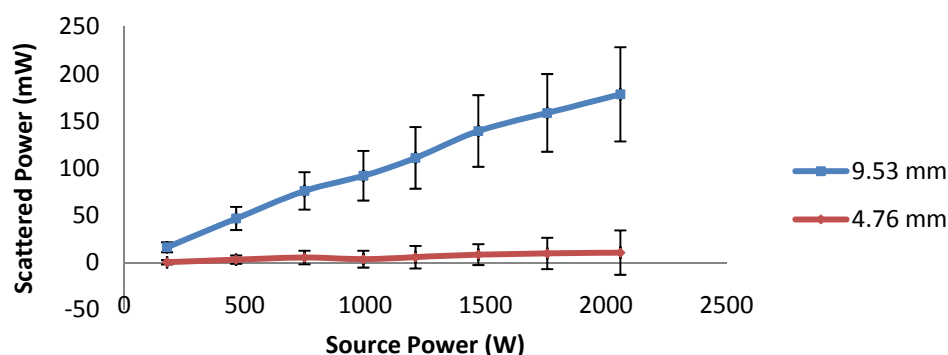


Figure 41: Scattered power versus source power for one aluminum sphere

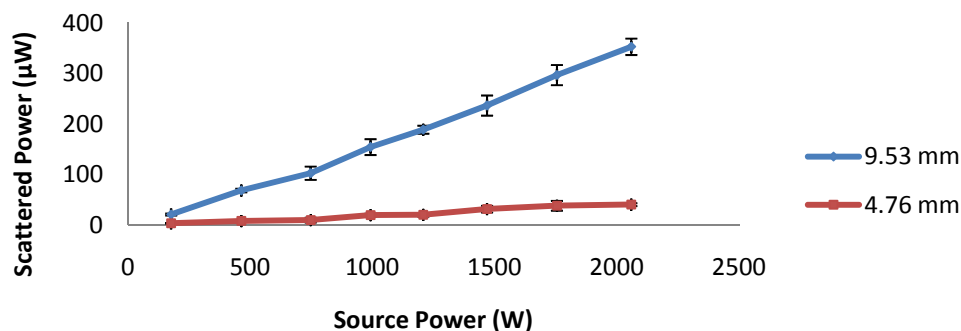


Figure 42: Scattered power versus source power for two aluminum spheres

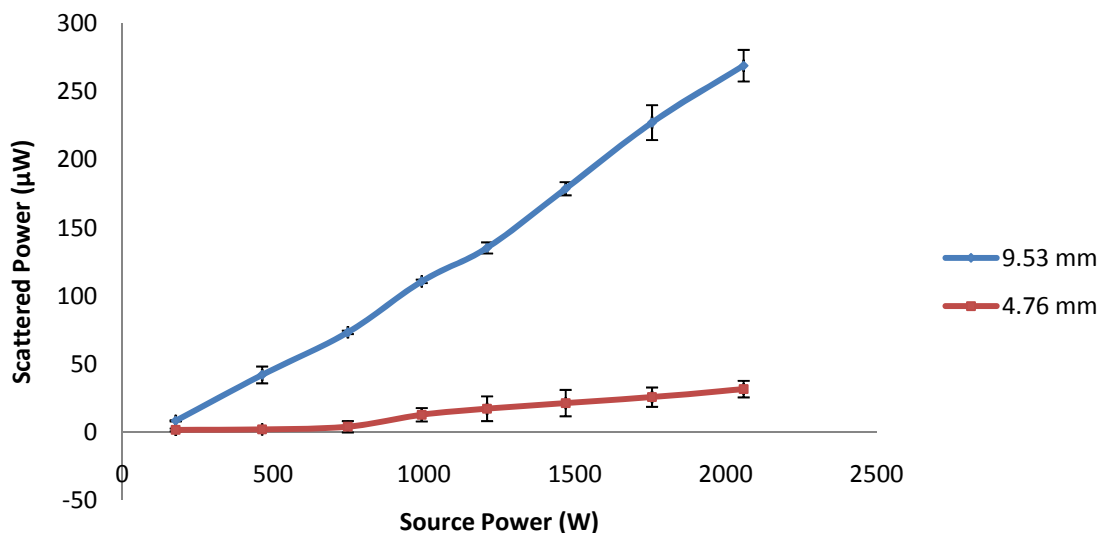


Figure 43: Scattered power versus source power for three aluminum spheres

As can be seen from the above figures, the expected doubling occurs between the single sphere and the double sphere tests. However, once a third sphere is added, the scattered signal actually decreases. This seems to be the result of inter-particle interactions which lead to a lower returned scattered signal. Drolen and Tien⁵⁷ investigated this phenomenon in regards to independent and dependent scattering in packed-sphere systems. They show that a dependent scattering system has a decreased scattering efficiency. This may be the cause for the decrease in the triple sphere scattered power. However, more tests would need to be conducted in order to confirm this. Also, it would also have to be determined if the environment inside in the solid rocket exhaust plume falls into either the independent regime or the dependent regime for scattering.

CHAPTER 9

CONCLUSION

This study has developed the notional plans for a real-time, non-intrusive diagnostic tool for the characterization of a solid rocket exhaust plume using Rayleigh scattering theory and terahertz radiation. This study has shown the feasibility of measuring particle size based on the collected Rayleigh scattered light if the particle number density, index of refraction, and scattering efficiency is known. Terahertz radiation has captivated many researchers because of its relatively unexplored nature and wide range of applications. It occupies the part of the spectrum between 100 GHz and 10 THz. Terahertz sources currently have relatively low output powers with a maximum in the tens of Watts. Despite these low powers, some terahertz sources have attained high intensity ratios based on Rayleigh scattering theory. A high output power is desired for the projections of this study. Thus, UCCS researchers are developing a compact gyrotron source that will operate at 300 GHz with an output power of 1 kW. This source can provide the necessary output for the notional terahertz diagnostic instrument.

The optical properties of alumina were researched with emphasis put on the index of refraction. It was determined that a dependence exists between the temperature of the particles and the wavelength of light for this property. Therefore, studies must be conducted in order to determine the index of refraction of alumina at terahertz frequencies at the temperatures experienced inside the rocket plume.

The equations for two elastic scattering theories were analyzed for application to this study. Mie theory was briefly discussed and can be applied to any spherical particle with any incident wavelength of light. Rayleigh theory which is an approximation of Mie theory can only be applied if the particle radius is ten times smaller than the wavelength. The intensity ratios for both theories depend on the particle radius, the number density, the wavelength of the incident light, and the index of refraction of the material. The intensity ratio from Rayleigh theory was resolved into an equation for determining the power received based on the dimensions of the detector and the experimental setup along with the particle radius, index of refraction, and wavelength of light. The issue of using one equation with two unknowns was discussed and a solution could lie in the use of a frequency sweeping source. By increasing the frequency one could

effectively turn off the scattered power of larger particles because of the nature of Rayleigh and Mie scattering. Using this technique, the scattering for groups of particles could be measured and their average sizes and number densities determined.

It was found that the trends of the data matched the expected general trends developed in the predictions. Best fit predicted lines were generated using Eq. (29) with a scattering efficiency of 100% and varying indices of refractions for the materials. The indices of refraction for aluminum, brass, and stainless steel were 3.4, 6.0, and 1.85 respectively. The percent differences were reported and found to be small for the assumed parameters, but grew with decreasing sphere radius. Many possible sources of error were presented which may have contributed to the differences. The most prominent of these error sources is the low signal to noise ratio produced by the tests. Also, the uncertainty surrounding the index of refraction and scattering efficiency contribute to the error.

The proof-of-concept experimental results paved the way for the development of a notional terahertz diagnostic instrument. First, Rayleigh theory was combined with free-space transmission equations and antenna theory for a parabolic reflector antenna. A general equation was generated for the power ratio for alumina particles inside a solid rocket exhaust plume. From this general equation, predictions were made for the performance of a notional terahertz instrument. The importance of frequency matching to particle size was highlighted in order to preserve the transmitted to received power ratio. Also, the predictions were shown for a system operating at 20 km away from the rocket plume with a 3 meter diameter parabolic dish antenna. Based on these predictions and the development of the 1 kW gyrotron source, the notional system was determined to be able to generate micro-Watts of scattered power at the given range using 3 meter diameter transmitting and receiving dishes.

Some complications that would arise in the development and application of an actual terahertz diagnostic instrument were analyzed. The largest complication to the operation of such a system would be atmospheric disturbances and attenuations. Water was recognized as the biggest hindrance to operation. From these problems it is recommended that an even higher power source be used preferably something in the MW range. Another problem would be in development of the antenna as far as construction, tracking capability, and efficiency. The last problem encountered is the effects of inter-particle interactions. Some

experimental data was presented showing the effect it can have in lowering the scattering efficiency. This issue would have to be addressed and characterized in order to use the terahertz instrument effectively.

This study has developed a notional non-intrusive, real-time diagnostic instrument using Rayleigh scattering and terahertz radiation. It has also shown the feasibility of such a device through a proof-of-concept experiment conducted at microwave frequencies with appropriately scaled particles. While issues will need to be addressed by future work in order to create and operate an actual diagnostic tool, many potential solutions are presented. A compact diagnostic instrument of this nature can have enormous potential in the future of characterizing the properties of solid rocket plumes.

REFERENCES

- ¹ Sambamurthi, Jay K. "Al₂O₃ Collection and Sizing from Solid Rocket Motor Plumes." *J. of Propulsion and Power*. Vol. 12, No. 3 pp. 598-604. May-June 1996.
- ² Zhang, X-C. "Terahertz imaging: horizons and hurdles," *Phys. Med. Biol.* 47, pp. 3667-3677. 2002.
- ³ Kim, K.J., M. E. Read, J. M. Baird, K. R. Chu, A. Drobot, J. L. Vomvoridis, A. Ganguly, D. Dialetis, V. L. Granatstein. "Design considerations for a megawatt CW gyrotron," *Int. J. Electron.*, vol. 51, pp. 427-45, 1981.
- ⁴ Seasholtz, R. G., F. J. Zupanc, and S. J. Schneider. "Spectrally Resolved Rayleigh Scattering Diagnostic for Hydrogen-Oxygen Rocket Plume Studies." *Journal of Propulsion and Power*. Vol. 8, No. 5. pp. 935-42. Sept.-Oct. 1992.
- ⁵ Simmons, Frederick S. *Rocket Exhaust Plume Phenomenology*. El Segundo, California: The Aerospace Press, 2000. pp. 193-200.
- ⁶ Mueller, Eric M. "Terahertz Radiation: Application and Sources." *The Industrial Physicist*. pp. 27-29. Aug-Sept. 2003.
- ⁷ Trager, Frank ed. *Springer Handbook of Laser and Optics*. Springer: New York, 2007.
- ⁸ Weber, Marvin J. *Handbook of Lasers*. CRC Press: Boca Raton, 2001.
- ⁹ Weber, Marvin J. *Handbook of Laser Science and Technology*. Supplement 1: Lasers. CRC Press: Boca Raton, 1991.
- ¹⁰ Weber, Marvin J. *Handbook of Laser Science and Technology*. Volume II: Gas Lasers. CRC Press: Boca Raton, 1991.
- ¹¹ Siegel, Peter H. "Terahertz Technology." *IEEE Transactions on Microwave Theory and Techniques*. Vol. 50. No. 3. pp. 910-28. March 2002.
- ¹² Gaidis, Micheal C. "Space-Based Applications of Far-Infrared Systems." *8th Int. Terahertz Electron.Conf.* pp. 125-128. Sept. 2000.
- ¹³ Hu, B. B. and M. C. Nuss. "Imaging with Terahertz Waves." *Optics Letters*. Vol 20. No. 16. pp. 1716-1718. Aug. 1995.
- ¹⁴ Liu, Hai-Bo, Hua Zhong, Nicholas Karpowicz, Yunqing Chen, and X.-C. Zhang. "Terahertz Spectroscopy and Imaging for Defense and Security Applications." *Proceedings IEEE*. **95**. pp. 1514-1527. 2007.
- ¹⁵ Bogue, Robert. "Terahertz Imaging: A Report on Progress." *Sensor Review*. Vol. 29 No. 1 pp. 6-12. 2009.
- ¹⁶ Granatstein, Victor L., Gregory S. Nusinovich, Monica Blank, Kevin L. Felch, Ronald M. Gilgenbach, Hezhong Guo, Howard Jory, Neville C. Luhmann, Jr., David B. McDermott, John M. Rodgers, and

-
- Thomas A. Spencer. *High-Power Microwave Sources and Technologies*. Barker, Robert J. and Edl Schamiloglu eds. New York: IEEE Press, 2001.
- ¹⁷ T. Mulcahy, H. Song, A. O'Shea, and A. Ketsdever, "Large Orbit Electron Gun for a High-Order Harmonic Terahertz Radiation Source," *The 37th EPS Conference on Plasma Physics*, Dublin, Ireland, 21-25 June 2010.
 - ¹⁸ Simmons, Frederick S. *Rocket Exhaust Plume Phenomenology*. El Segundo, California: The Aerospace Press, 2000. pp. 29-30.
 - ¹⁹ Simmons, Frederick S. *Rocket Exhaust Plume Phenomenology*. El Segundo, California: The Aerospace Press, 2000. pp. 99-112.
 - ²⁰ Owis, Farouk M. and Ali. A. Hashem. "Numerical Computations of Two-Phase Flow in Small Thrusters for Satellite Control." *AIAA Paper* 2003-4263.
 - ²¹ Krishnan, Shankar, J. K. Richard Weber, Robert A. Schiffman, and Paul C. Nordine. "Refractive Index of Liquid Aluminum Oxide at 0.6328 μm ." *J. Am. Ceram. Soc.* **74** [4] pp. 881-83. 1991.
 - ²² Gupta R. P. and T. F. Wall. "The Complex Refractive Index of Particles." *J. Phys. D: Appl. Phys.* **14**. L95-8. 1981.
 - ²³ Gryvnak, David A. and Darrell E. Burch. "Optical and Infrared Properties of at Elevated Temperatures." *Journal of the Optical Society of America*. Vol. 55 No. 6. pp. 625-29. June 1965.
 - ²⁴ Malitson, Irving H., Frederick V. Murphy, Jr., and William S. Rodney. "Refractive Index of Synthetic Sapphire." *J. Opt. Soc. Am.* Vol. 48. pp. 72-3. January 1958.
 - ²⁵ Plass, Gilbert N. "Temperature Dependence of the Mie Scattering and Absorption Cross Sections for Aluminum Oxide." *Applied Optics*. Vol. 4, No. 12. pp. 1616-1619. December 1965.
 - ²⁶ Hermesen, R. W. "Aluminum Oxide Particle Size for Solid Rocket Motor Performance Prediction." *J. Spacecraft*. Vol. 18, No. 6. pp. 483-90. 1981.
 - ²⁷ Laredo, D., J. D. McCrorie II, J. K. Vaughn, and D. W. Netzer. "Motor Plume Particle Size Measurements in Solid Propellant Micromotors." *Journal of Propulsion and Power*. Vol. 10, No. 3. pp. 410-418. 1994.
 - ²⁸ Kobalev, Oleg B. "Motor and Plume Particle Size Prediction in Solid-Propellant Rocket Motors." *Journal of Propulsion and Power*. Vol. 18, No. 6. pp. 1199-1210. 2002.
 - ²⁹ Beiting, Edward J. "Predicted Physical and Optical Characteristics of Solid Rocket Motor Exhaust in the Stratosphere." *AIAA Paper* 97-0532.
 - ³⁰ An-Le, Lei, Zhai Hua-Jin, Liu Bing-Chen, Li Zhong, Ni Guo-Yuan, Xu Zhi-Zhan. "Size Determination of Argon Clusters from a Rayleigh Scattering Experiment." *Chinese Physical Letters*. Vol. 17, No. 9. pp. 661-662. 2000.
 - ³¹ Seasholtz, R. G., F. J. Zupanc, and S. J. Schneider. "Spectrally Resolved Rayleigh Scattering Diagnostic for Hydrogen-Oxygen Rocket Plume Studies." *Journal of Propulsion and Power*. Vol. 8, No. 5. pp. 935-942. Sept.-Oct. 1992.
 - ³² Zupanc, Frank J. "Pulsed Laser Rayleigh Scattering Diagnostic for Hydrogen/Oxygen Rocket Exit Plane Flowfield Velocimetry." *AIAA Paper* 93-0805.

-
- ³³ Seasholtz, Richard G., Alvin E. Buggele, and Mark F. Reeder. "Flow Measurements Based on Rayleigh Scattering and Fabry-Perot Interferometer." *Optics and Lasers in Engineering*. **27**. pp. 543-570. 1997.
- ³⁴ Panda, J. and R. G. Seasholtz. "Velocity and Temperature Measurement in Supersonic Free Jets Using Spectrally Resolved Rayleigh Scattering." *NASA/TM* 2004-212391.
- ³⁵ Zhang, Shu Zhen, Feng Lin Zhao, Ke An Li, Shen Yang Tong. "Determination of glycogen by Rayleigh light scattering." *Analytica Chimica Acta*. Vol. 431. pp. 133-139. 2001.
- ³⁶ Shneider M. N. and R. B. Miles. "Microwave diagnostics of small plasma objects." *J. of Applied Physics*. **98**. pp. 033301-1 - 033301-3. 2005.
- ³⁷ Zhang, Zhili, Mikhail N. Shneider, and Richard B. Miles. "Microwave Diagnostics of Laser-Induced Avalanche Ionization in Air." *Journal of Applied Physics*. **100**. pp. 074912-1-6. 2006.
- ³⁸ Zhang, Zhili, Mikhail N. Shneider, and Richard B. Miles. "Coherent Microwave Rayleigh Scattering from Resonance-Enhanced Multiphoton Ionization in Argon." *Physical Review Letters*. Vol. 98, pp. 265005-1 - 265005-4. 2007.
- ³⁹ Van de Hulst, H. C. *Light Scattering by Small Particles*. New York: John Wiley and Sons, 1957. pp. 114-130.
- ⁴⁰ Miles, Richard B., Walter R. Lempert, Joseph N. Forkey. "Laser Rayleigh Scattering." *Meas. Sci. Technol.* **12** R33-R51. 2001.
- ⁴¹ Van de Hulst, H. C. *Light Scattering by Small Particles*. New York: John Wiley and Sons, 1957. pp. 85-93.
- ⁴² Ulaby, Fawwaz T. *Fundamentals of Applied Electromagnetics*. Upper Saddle River, NJ: Pearson Prentice Hall, 2007.
- ⁴³ Horvath, H. "Atmospheric Light Absorption – A Review." *Atmospheric Environment*. Vol. 27A, No. 3. pp. 293-317. 1993.
- ⁴⁴ Petty, Kevin R. and William P. Mahoney III. "Weather Applications and Products Enabled Through Vehicle Infrastructure Integration." *U.S. Dept. of Transportation: Federal Highway Administration*. Report No. FHWA-HOP-07-084. January 2007.
- ⁴⁵ Stutzman, Warren L. and Gary A. Thiele. *Antenna Theory and Design*. New York: John Wiley and Sons, 1981. pp. 17.
- ⁴⁶ Stutzman, Warren L. and Gary A. Thiele. *Antenna Theory and Design*. New York: John Wiley and Sons, 1981. pp. 24.
- ⁴⁷ Love, A.W. "Some Highlights in Reflector Antenna Development." *Reflector Antennas*. Love, A. W. ed. New York: IEEE Press, 1978.
- ⁴⁸ Jones, E. M. T. "Paraboloid Reflector and Hyperboloid Lens Antenna." *Reflector Antennas*. Love, A. W. ed. New York: IEEE Press, 1978.
- ⁴⁹ Larson, Wiley J. and James R. Wertz ed. *Space Mission Analysis and Design*. El Segundo, California: Microcosm Press, 1999.
- ⁵⁰ Stutzman, Warren L. and Gary A. Thiele. *Antenna Theory and Design*. New York: John Wiley and Sons, 1981. pp. 397-415.

-
- ⁵¹ Cox, A. J., Alan J. Deweerd, and Jennifer Linden. "An Experiment to Measure Mie and Rayleigh Total Scattering Cross Sections." *Am. J. Phys.* **70**. pp. 620-625. 2002.
- ⁵² Kovalev, O. B. "Prediction of the Size of Aluminum-Oxide Particles in Exhaust Plumes of Solid Rocket Motors." *Combustion, Explosion, and Shock Waves*. Vol. 38, No. 5. pp. 535-546. 2002.
- ⁵³ Farmer, W. M. "Measurement of Particle Size, Number Density, and Velocity Using a Laser Interferometer." *Applied Optics*. Vol. 11, No. 11. pp. 2603-2612. November 1972.
- ⁵⁴ Shiles, E., T. Sasaki, M. Inokuti, Y. D. Smith. "Self-consistency and Sum-rule Tests in the Kramers-Kronig Analysis of Optical Data: Applications to Aluminum." *Phys. Rev. Sect. B*. Vol. 22, No. 4. pp. 1612-1628. 1980.
- ⁵⁵ Van de Hulst, H. C. *Light Scattering by Small Particles*. New York: John Wiley and Sons, 1957. pp. 158
- ⁵⁶ Cornella, Barry, Andrew Ketsdever, Natalia E. Gimelshein and Sergey F. Gimelshein. "Thrust Augmentation of Solid Rocket Motors Using Beamed Microwave Energy." *J. Propulsion and Power*. Accepted 2010.
- ⁵⁷ Drolen, B.L. and C.L. Tien. "Independent and Dependent Scattering in Packed-Sphere Systems." *J. Thermophysics*. Vol. 1, No. 1. pp. 63-68. 1987.

APPENDIX A: ROCKET PLUME CONSTITUENT DATA

Item No.	RUSS	Propellant	Test No.	ξ_T	T_{ex} , °K	\bar{P}_{ex} , psia	D_{ex} , in.	M_0/M_T	T_{ex} , °K	D_{ex} , cm	α^{**}	Collection Method	Measurement Method	Reference
1.*	134-3	LPC-383A 87% solid PRAN	18	0.32	6260	667	40.4	0.5	113	10.9	0.22	1	OH	12,13,14
2.*	134-4	LPC-383C 87% solid PRAN	18	0.32	6260	664	34.3	0.6	110	11.1	0.22	1	OH	12,13,14
3.	134-7	TP-81153 86% solid PRAN	16	0.26	6110	360	20.0	1.0/1.0	143	10.8	0.205	1	OH	12,13,14
4.	134-9	TP-81115 87% solid PRAN	18	0.32	6400	360	34.3	0.9/0.8	110	12.0	0.25	1	OH	13,14
5.	YOC-120	TP-81085 88.3% solid CTPB	20	0.34	6260	700	34.3	0.9/0.5	182	11.1	0.20	1	OH	12,13
6.*	YOC-120	TP-81077 86% solid PRAN	16	0.26	6110	---	21.3	---	---	8.5	---	1	OH	12
7.	UA-1285	UTP-3001 84% solid PRAN	16	0.285	5860	530	17.7	0.4	175	12.0	0.17	2,3,6	OH,SH	12,13,14
8.	160-SL2	AMP-3235 83% solid PRAN	15	0.26	5990	489	71.0	1.0	202	12.9	0.22	1	OH	12,13
9.*	160-SL3	AMP-3254 83% solid PRAN	15	0.26	5990	539	89.3	0.7	143	13.3	0.23	1	OH	13,14
10.	44824	AMP-3254 83% solid PRAN	15	0.26	5990	445	15.3	0.79/1.0	23	6.89	---	2	OH	13
11.*	Powder/P3	TP-81114 86% solid PRAN	16	0.26	6110	870	11.6	1	154	8.75/8.2	---	2	OH	13
12.*	HW/IS- Wing II	AMP-2864 82% solid PU	17	0.293	6090	460	8.3	3	60.3	5.8	---	2	OH	13
13.	Super BATES	UTP-18,803A 90% solid HTPB	21	0.357	6570	1,060	8.0	2	74	5.23	0.35	5	SE	17
14.	HW/IS 65-in.	TP-81011 86% solid PRAN	16	0.26	6110	634	7.5	1	91	8.98	0.35	1	OH	12
15.	45-in.	UTP-15,908 90% solid HTPB 232 OH	18	0.305	6320	930	4.14	4	143	6.23	0.24	5	SH	22
16.	CA/TS ADP	UTP-15,908 90% solid HTPB 232 OH	18	0.305	6320	1,000	4.04	4	90	6.17	0.21	5	SH	22
17.	HW/IS ADP	UTP-15,908 90% solid HTPB 232 OH	18	0.297	6770	1,210	6.81	2/1	137	5.77	0.21	5,8	SE	14
18.†	76-in.	AMP-3236	---	---	---	---	---	---	---	6.10	---	2	OH	13
19.†	Shuttle Staging Motor	UTP-19,048 86% solid HTPB	2	0.036	5390	1,700	3.2	1.5	4.5	1.54	0.18	3	SH	22
20.	CSB-TN-3	UTP-15,131 90% solid HTPB 232 OH	18	0.303	6280	770	1.3	2	54	5.33	0.22	4	SH	22
21.	CSB-TN-3	UTP-15,131 90% solid HTPB 232 OH	18	0.305	6320	1,093	1.04	2	44	4.36	0.32	3	SH	22
22.	CSB-TN-3	UTP-15,908 90% solid HTPB 232 OH	18	0.305	6320	980	1.03	2	68	5.36	0.21	5	SH	22
23.*	70-1b BATES	HW-P-112 43% solid CHB	20	0.271	6140	1,200	2.1	2	16	2.63	---	2	EH	13
24.†	70-1b BATES	HW-P-112 43% solid CHB	20	0.271	5960	460	1.73	2	5.2	5.41	---	2	EH	13
25.	70-1b BATES	AMP-2949 73% solid PU	20	0.34	6440	1,000	1.38	2	35	2.32	---	2	EH	13
26.†	70-1b BATES	AMP-3044 86% solid CTPB	13	0.25	6290	1,000	1.76	2	27	1.93	---	2	EH	13
27.	70-1b BATES	TP-8-1120 86% solid PRAN	16	0.26	6125	500	3.21	2	6.9	2.72	---	2	EH	13
28.*	70-1b BATES	TP-8-8163 86% solid PRAN	16	0.26	6240	1,000	2.80	2	18	2.11	---	2	EH	13
29.	70-1b BATES	TP-8-8163 86% solid PRAN	16	0.26	6110	550	2.46	2	12	2.00	---	2	EH	13
30.*	70-1b BATES	LPC-383A 87% solid PRAN	18	0.32	6330	1,000	2.52	2	13	2.46	---	2	EH	13
31.	WCF-5-17.1	HW-P-170 54% solid CHB	22	0.38	6670	1,000	1.70	2	17	2.40	---	2	EH	13
32.†	WCF-5-17.1	HW-SE-108 63% solid TPOA	13	0.25	6380	1,000	1.70	2	16	1.90	---	2	EH	13

Item No.	Motor	Prevalant	\bar{L} AE	\bar{L}_c	$\bar{L}_{c,0}$	$\bar{L}'_{c,0}$	$\bar{L}'_{c,0}$	$\bar{L}_{c,0}/\bar{L}$	$\bar{L}_{c,0}/\bar{L}$	$\bar{L}_{c,0}/\bar{L}$	$\bar{L}_{c,0}/\bar{L}$	$\bar{L}_{c,0}/\bar{L}$	Collection Method	Measurement Method	Reference
33.*	1000-1000	812 anilide polyurethane	17	0.292	6050	1,000	1.9	2	31	4.58	---	7	EM	18	
34.*	300-1000	812 anilide polyurethane	17	0.292	6050	1,000	0.9	2	19	4.43	---	7	EM	18	
35.*	↑	↑	17	0.31	5580	900	1.6	2	5	3.2	---	7	EM	18	
36.	↓	↓	15	0.218	5900	1,000	0.9	2	13	4.33	---	7	EM	18	
37.	↓	↓	19	0.328	6340	1,000	0.9	2	13	4.48	---	7	EM	18	
38†	300-1000	812 anilide polyurethane	3	0.052	5120	1,000	0.9	2	12	3.11	---	7	EM	18	
39†	100-250	812 anilide polyurethane	17	0.293	6010	1,000	0.3	2	6	0.73	---	7	EM	18	
40†	100-210	812 anilide polyurethane	3	0.052	5120	1,000	0.3	2	5	0.25	---	7	EM	18	
41.	80-5PC	DEP-08 412 anilide CMBS	20.9	0.368	7020	1,000	0.8	2	6.3	3.12	0.396	3	EM	21	
42.	↓	↓	↓	↓	6980	800	0.95	2	4.6	3.23	0.372	3	EM	21	
43.	80-5PC	DEP-08 412 anilide CMBS	20.9	0.368	6920	800	1.1	2	3.4	3.21	0.402	3	EM	21	
44.*	300-500	AM-1254 812 anilide PMAN	15	0.26	4040	1,000	1.8	0.3	3.9	2.33	---	2	EM	19	
45.*	15-100 MATES	80-0-112 412 anilide CMBS	20	0.271	6180	1,000	1.20	2	8.3	2.19	---	2	EM	19	
46.	CSD-TN-1	UTP-15, 908 902 anilide HTPB 158 HMX	18	0.309	6340	1,116	0.70	2	23	4.99	0.20	5	SH	22	
47.	CSD-TN-1	UTP-15, 908 902 anilide HTPB 158 HMX	18	0.309	6350	1,348	0.65	2	29	4.76	0.21	5	SH	22	
48.	CSD-TN-1	UTP-13, 945 882 anilide HPTB	18	0.315	6330	685	1.31	2	7.1	2.61	0.10	4	SH	22	
49.	CSD-4 10	UTP-13, 475 882 anilide CTPB	18	0.289	6430	1,080	0.629	2	11.7	3.00	0.16	4	SH	22	
50.	CSD-4 1b	UTP-13, 945 882 anilide HTPB	18	0.313	6300	997	0.639	2	6.8	3.56	0.18	4	SH	22	
51.	CSD-4 1b	UTP-15, 158 902 anilide HTPB 148 HMX	16.5	0.28	6130	1,080	0.598	2	10.7	2.66	0.20	4	SH	22	
52.	CSD-4 1b	UTP-13, 908 902 anilide HTPB 158 HMX	18	0.335	6530	1,030	0.344	2	15.8	3.06	0.10	5	SH	22	
53†	CSD-3C3-2	UTP-1096 842 anilide PMAN	16	0.277	6030	1,180	0.29	2	67	4.09	0.15	3	EM	19	
54.	↑	↑	16	0.277	6060	1,080	0.58	2	67	4.08	0.33	3	EM	19	
55.	↑	↑	16	0.277	5960	630	0.38	2	68	3.64	0.19	3	EM	19	
56†	↑	↑	16	0.270	5840	119	0.56	2	71	0.52	0.22	3	EM	19	
57.	↑	↑	16	0.277	6030	800	0.50	2	32	3.23	0.33	3	EM	19	
58.	↑	↑	16	0.277	5980	730	0.50	2	33	2.94	0.29	3	EM	19	
59.	↑	↑	16	0.275	5880	149	0.50	2	35	1.84	0.24	3	EM	19	
60.	↑	↑	16	0.277	6030	980	0.50	2	34	2.99	0.33	3	EM	19	
61.	↑	↑	16	0.277	5930	850	0.50	2	33	2.68	0.38	3	EM	19	
62.	↑	↑	16	0.276	5930	430	0.58	2	35	2.80	0.19	3	EM	19	
63.	↑	↑	16	0.27	5840	100	0.58	2	37	0.93	0.26	3	EM	19	
64.	CSD-3C3-2	UTP-1096 842 anilide PMAN	16	0.274	5760	190	1.08	2	8	1.05	0.27	3	EM	19	
65.	CSD-3C3-2	UTP-4574 812 anilide PMAN	5	0.081	5268	680	0.50	2	15	1.85	0.31	3	EM	20	
66.	DC1.5-4	UTP-13, 945 882 anilide HTPB	18	0.315	6340	997	0.319	2	4.1	2.48	0.25	4	SH	22	

* Indicates data was included in original DEP correlation, Reference 30.

† Standard deviation of $\log_{10} \bar{L}$ on log-normal distribution. Calculated from original particle counts.

‡ Data not used in final correlation.

Collection Method

1. 80-5F sampler with LAGI sampler
2. Petri dishes
3. Closed tank
4. BOMAS pool collector
5. CSD probe
6. U-2 with BOMAS sampler
7. Wetted plate collector
8. RFI box collector

Measurement Method

0. optical microscope
1. transmission electron microscope
2. scanning electron microscope
3. measured and counted manually
4. image analyzer

APPENDIX B: MATLAB CODE FOR EXPERIMENTAL PREDICTIONS

```
%%%%%%%%%%%%%%%%%%%%%%%%%%%%%%%%%%%%%%%%%%%%%%%%%%%%%%%%%%%%%%%%%%%%%%%%
% Microwave_Rayleigh_Predictions_2kW
%
% This script calculates the received Rayleigh scattered power from a
% variety of different ball sizes and materials based on user inputs.
% It then plots the results as scattered power vs source power
% and scattered
% power versus particle radius.
%
% Author: Anthony O'Shea
%
% Inputs:
%   Parameters of experiment
%
% Outputs:
%   Pr - the scattered power received
%
% Globals:  None
%
% Constants: None
%
% Coupling: None
%
% References: 40 and 41
%%%%%%%%%%%%%%%%%%%%%%%%%%%%%%%%%%%%%%%%%%%%%%%%%%%%%%%%%%%%%%%%%%%%%%%%

%clear all
%clc
%Define variables for integration
syms theta phi
%Define Sphere Radii
r = [0.75/2*2.54/100,0.625/2*2.54/100,0.5/2*2.54/100,0.375/2*2.54/100];
%r = [0.75/2*2.54/100,0.375/2*2.54/100];
%Set Input Power
Pt = [100,400,700,1000,1300,1600,1900,2100];
%Input Experimental Setup Parameters
H = 4.875;
W = 6.25;
D = 56;
T = 121.75;
L = 122;
C1 = 96.25;
C2 = 121.5;
thetac = acos(D^2-C1^2-C2^2+2*C1*C2);
thetaa = asin(W/2/L);
phia = asin(H/2/T);
phi1 = pi/2-phia;
phi2 = pi/2+phia;
theta1 = thetac-thetaa;
theta2 = thetac+thetaa;
%Set Index of Refraction and Scattering Efficiency
%m = 1.39;
%m = 2.0016;
%m = 2.50;
```

```

m = 10^9;
eta = .25;
%Input Antenna Gains and Wavelength
dB1 = 10;
dB2 = 14.17;
lambda = 0.1224;
%Define cross-sectional area of sphere
R = C1*2.54/100;
%Setup iteration loop
Pr = zeros(8,1);
count = 0;
for j = 1:4
    rp = r(j);
    %Calculate sphere volume
    V = 4/3*pi*rp^3;
    for n = 1:8
        Ph = Pt(n);
        %Calculate differential scattering cross-section
        sigss = 9*pi^2*V^2*((m^2-1)/(m^2+2))^2*...

int(int((sin(phi))^3,phi,phi1,phi2),theta,theta1,theta2)/...
        lambda^4;
        %Calculate the power received
        %Pr(n,j) = 10^(dB1/5)*(lambda/(4*pi*R))^2*sigss/(pi*rp^2)*Ph;
        Pr(n,j) = eta*2*10^(dB1/10)*10^(dB2/10)*(lambda/(4*pi*R))^2*...
            sigss/(pi*rp^2)*Ph;
        count = count+1
    end
end
%Generate plot for scattered power versus source power
plot(Pt,Pr(:,1),'k')
hold on
plot(Pt,Pr(:,2),'--k')
plot(Pt,Pr(:,3),'-.k')
plot(Pt,Pr(:,4),' :k')
legend('r = 9.53 mm','r = 7.94 mm','r = 6.35 mm','r = 4.76 mm')
%legend('r = 9.53 mm','r = 4.76 mm')
hold off
Pr
%Generate plot for scattered power versus sphere radius
figure(2)
plot(r,Pr(8,:))

```

APPENDIX C: MATLAB CODE FOR THZ INSTRUMENT PERFORMANCE

```
%%%%%%%%%%%%%%%%%%%%%%%%%%%%%%%%%%%%%%%%%%%%%%%%%%%%%%%%%%%%%%%%%%%%%%%%
% Terahertz_Rayleigh
%
% This script calculates the Rayleigh power ratio from a
% notional terahertz instrument and alumina particles.
% It then plots the results as scattered power versus source power
% and scattered power versus particle radius.
%
% Author: Anthony O'Shea
%
% Inputs:
%   Parameters of notional instrument
%
% Outputs:
%   ratio - the Rayleigh power ratio
%
% Globals:  None
%
% Constants: None
%
% Coupling: None
%
% References: 40 and 41
%%%%%%%%%%%%%%%%%%%%%%%%%%%%%%%%%%%%%%%%%%%%%%%%%%%%%%%%%%%%%%%%%%%%%%%%
clear all
clc
%Define variables for integration
syms theta phi
r = 100e-6; %Radius of particle (m)
lambda = 3e8/300e9; %Wavelength (m)
V = (4/3)*pi*r^3; %Volume of particle (m^3)
m = 1.76; %Index of refraction
%Set up for loop
ratio = zeros(100,1);
R = zeros(100,1);
count = 0;
%Define radius of dish (m)
rdish = [0.5,0.75,1,1.25,1.5];
%rdish = [1.5,1.25,1,0.75,0.5];
Rmax = 30000;
%Run iterative loop
for j = 1:5
    rd = rdish(j);
    for n = 1:100
        count = count+1
        %Calculate minimum distance based on far-field criteria
        Rmin = 2*(2*rd)^2/0.001;
        R(n,j) = Rmin+(n-1)*(Rmax-Rmin)/100;
        %Calculate antenna gain
        dB = 17.8+20*log10(2*rd)+20*log10(300);
        %Determine integral bounds for Rayleigh theory
        phi1 = pi/2-atan(rd/R(n,j));
        phi2 = pi/2+atan(rd/R(n,j));
        theta1 = pi/4-atan(rd/R(n,j));
```

```

        theta2 = pi/4+atan(rd/R(n,j));
        %Calculate differential scattering cross-section
        sigss = 9*pi^2*V^2*((m^2-1)/(m^2+2))^2*...

int(int((sin(phi))^3,phi,phi1,phi2),theta,theta1,theta2)/lambda^4;
        %Calculate ratio between scattered power and source power
        ratio(n,j) =
10^(dB/5)*(lambda^2/(4*pi*R(n,j)))^2*sigss/(pi*r^2);
    end
end
%Plot results
plot(R(:,1),ratio(:,1),'-')
hold on
plot(R(:,2),ratio(:,2),'-.')
plot(R(:,3),ratio(:,3),':')
plot(R(:,4),ratio(:,4),'--')
plot(R(:,5),ratio(:,5),'-')
hold off

```